

Dynamics of Quark-Gluon-Plasma Instabilities in Discretized Hard-Loop Approximation

Anton Rebhan,¹ Paul Romatschke,² and Michael Strickland^{1,3}

¹*Institut für Theoretische Physik, Technische Universität Wien,
Wiedner Hauptstrasse 8-10, A-1040 Vienna, Austria*

²*Fakultät für Physik, Universität Bielefeld, D-33501 Bielefeld, Germany*

³*Helsinki Institute of Physics*

P.O. Box 64, FIN-00014 University of Helsinki, Finland

(Dated: February 2, 2008)

Non-Abelian plasma instabilities have been proposed as a possible explanation for fast isotropization of the quark-gluon plasma produced in relativistic heavy-ion collisions. We study the real-time evolution of these instabilities in non-Abelian plasmas with a momentum-space anisotropy using a hard-loop effective theory that is discretized in the velocities of hard particles. We extend our previous results on the evolution of the most unstable modes, which are constant in directions transverse to the direction of anisotropy, from gauge group $SU(2)$ to $SU(3)$. We also present first full 3+1-dimensional simulation results based on velocity-discretized hard loops. In contrast to the effectively 1+1-dimensional transversely constant modes we find subexponential behavior at late times.

I. INTRODUCTION

If a quark-gluon plasma has been produced in the current heavy-ion-collider experiments at RHIC, the early onset of hydrodynamic behavior indicates so fast thermalization, or at least isotropization, that perturbative scattering processes alone do not seem to be capable of explaining it [1, 2, 3, 4, 5]. A number of nonperturbative scenarios have been put forward to account for the seemingly inevitable intrinsic strong-coupling nature of the quark-gluon plasma [6, 7, 8, 9]. However, a possible nonperturbative effect that does not rely on specifically strong-coupling physics, and that has not yet been fully taken into account in the available weak-coupling analyses, is the important collective dynamics arising from non-Abelian plasma instabilities, which are generalizations of the so-called Weibel or filamentary instabilities in ordinary electromagnetic plasmas [10]. Such instabilities are present already in *collisionless* plasmas with any amount of momentum anisotropies [11, 12], and, indeed, they have been found to play an important role in the fast isotropization of electromagnetic plasmas [13]. Their non-Abelian versions have been proposed to be of relevance for the quark-gluon plasma early on by Mrówczyński and others [14, 15, 16, 17, 18, 19], and specifically as explanation for the recent puzzle of fast apparent thermalization by Arnold, Lenaghan, Moore, and Yaffe [20, 21].

At weak coupling, the asymptotic regime where perturbative QCD becomes justifiable, there is a separation of scales between the scale pertaining to hard particles forming the nearly collisionless constituents of a plasma and the scale which is down by one power of the QCD coupling g , determining for example electrical screening masses. The wave vectors and growth rates of Weibel instabilities are of the same order, which is parametrically much larger than perturbative collision rates or even the parametrically larger color relaxation

rate. The degrees of freedom at the scale $g p_{hard}$ are to leading order described by a non-local and non-linear effective action called the hard-thermal-loop effective action [22] in the case of thermal equilibrium, and this has a simple generalization to plasmas with arbitrary momentum-space anisotropy [23].

In the static limit, the anisotropic hard-loop effective action has a potential which is unbounded from below. Using a static approximation and restricting to modes with momenta in the direction of anisotropy, upon which the hard-loop effective action becomes Gaussian and local, the evolution of plasma instabilities has been studied numerically by Arnold and Lenaghan in Ref. [24]. Based on these results, these authors have conjectured that non-Abelian plasma instabilities Abelianize in the regime of nonperturbatively large amplitudes, and thus grow exponentially like their Abelian counterparts as long as the assumptions of the hard-loop approximation hold. At parametrically larger gauge-field amplitudes $A \sim p_{hard}/g$, when they begin to have non-perturbatively large effects on the hard particles' trajectories, these modes are expected to eventually saturate by isotropizing the hard particle distribution.¹

The full hard-loop effective action, however, is nonlocal and nonlinear. Using an auxiliary-field formalism to make it local and discretizing with respect to the velocity space of the hard particles, we have carried out a full hard-loop simulation for an SU(2) plasma in Ref. [25] using initial conditions that like those considered in Ref. [24] are constant with respect to the spatial directions transverse to the anisotropy axis. These configurations evolve 1+1-dimensionally and contain the most unstable modes for a given longitudinal momentum. We found that there is subexponential behavior when the instabilities reach nonlinear amplitudes, but exponential growth roughly equal to that of the linear regime was restored deeper into the nonlinear regime. However, the instabilities of the full hard-loop effective theory do not exhibit global Abelianization as in the simplified model of Ref. [24], but only in limited domains with extent comparable to the wavelength of maximal growth.

In this paper we give a fuller account of these numerical simulations and we present their extension to the gauge group SU(3) of QCD. After introducing the local auxiliary-field formulation of the hard-loop effective theory in Sect. II, we introduce our method to discretize hard-loop momenta in Sect. III and compare with continuum results for the dispersion laws in Sect. IV. In Sect. V, we study the effectively 1+1-dimensional evolution of initial configurations with random fluctuations in the spatial direction of anisotropy, but which are constant with respect to transverse directions. We analyse discretization effects and the effect of upgrading the gauge group SU(2) to SU(3). In Sect. VI we finally consider initial conditions that are non-constant in the transverse direction and thus require full 3+1-dimensional simulations. While at the beginning of the nonlinear regime we obtain results similar to the effectively 1+1-dimensional simulations, we observe subexponential behavior deeper into the nonlinear regime, in qualitative agreement with a most recent 3+1-dimensional study by Arnold et al. [26] using a different discretization method. Sect. VII contains our conclusions.

¹ This important aspect has recently been studied in Ref. [32] for non-Abelian plasma instabilities. Our objective here is to investigate the hard-loop dynamics preceding (in a weak-coupling regime) the regime where backreaction needs to be included.

II. HARD-LOOP EFFECTIVE FIELD EQUATIONS FOR ANISOTROPIC PLASMAS

At weak gauge coupling g , there is a separation of scales in hard momenta $|\mathbf{p}| = p^0$ of (ultrarelativistic) plasma constituents, and soft momenta $\sim g|\mathbf{p}|$ pertaining to collective dynamics such as Debye screening, finite plasma frequency, and, in anisotropic plasmas, magnetic instabilities. The effective field theory for the soft modes that is generated by integrating out the hard plasma modes at one-loop order and in the approximation that the amplitudes of the soft gauge fields obey $A_\mu \ll |\mathbf{p}|/g$ is that of gauge-covariant collisionless Boltzmann-Vlasov equations [27]. In equilibrium, the corresponding (nonlocal) effective action is the so-called hard-thermal-loop effective action [22] which has a simple generalization to plasmas with anisotropic momentum distributions [23]. At the expense of introducing a continuous set of auxiliary fields, the hard-loop effective field equations can be made local in space and time. These field equations then involve an induced current of the form [18, 28]

$$j^\mu[A] = -g^2 \int \frac{d^3p}{(2\pi)^3} \frac{1}{2|\mathbf{p}|} p^\mu \frac{\partial f(\mathbf{p})}{\partial p^\beta} W^\beta(x; \mathbf{v}) \quad (1)$$

with a set of auxiliary fields $W_\beta(x; \mathbf{v})$ for each spatial unit vector appearing in the velocity $v^\mu = p^\mu/|\mathbf{p}| = (1, \mathbf{v})$ of a hard (ultrarelativistic) particle with momentum p^μ . The W 's satisfy

$$[v \cdot D(A)]W_\beta(x; \mathbf{v}) = F_{\beta\gamma}(A)v^\gamma. \quad (2)$$

with $D_\mu = \partial_\mu - ig[A_\mu, \cdot]$.

The equations are closed by the non-Abelian Maxwell equations

$$D_\mu(A)F^{\mu\nu} = j^\nu, \quad (3)$$

where $\nu = 0$ is the Gauss law constraint.²

In the following we shall consider the special case of cylindrically symmetric anisotropies in momentum space, so that there is only one direction of anisotropy, which in heavy-ion collision would be given by the collision axis. We can then parametrize $f(\mathbf{p}) = \tilde{f}(|\mathbf{p}|, p^z)$ and write

$$\begin{aligned} \frac{\partial f(\mathbf{p})}{\partial p^\beta} &= \frac{\partial \tilde{f}(|\mathbf{p}|, p^z)}{\partial |\mathbf{p}|} \frac{p^b \delta_{b\beta}}{|\mathbf{p}|} + \frac{\partial \tilde{f}(|\mathbf{p}|, p^z)}{\partial p^z} \delta_{z\beta} \\ &\equiv -\tilde{f}_1(|\mathbf{p}|, p^z) \frac{p^b \delta_{b\beta}}{|\mathbf{p}|} - \tilde{f}_2(|\mathbf{p}|, p^z) \delta_{z\beta}. \end{aligned} \quad (4)$$

Eq. (2) allows us to impose $p^\beta W_\beta = 0$, which leads to

$$j^\mu(x) = \frac{1}{2}g^2 \int \frac{d^3p}{(2\pi)^3} v^\mu [\tilde{f}_1 W^0(x; v) + \tilde{f}_2 W^z(x; v)]. \quad (5)$$

Notice that in the isotropic case one has $\tilde{f}_2 = 0$, and only W^0 appears, whose equation of motion (2) involves only electric fields. In the anisotropic case, however, W^z enters, whose equation of motion contains the z component of the Lorentz force.

² Our metric convention is $(+ - - -)$.

The induced current (1) is covariantly conserved for arbitrary momentum-space distribution functions f as can be verified by partial integration with respect to p^β [23]. In the case of a parity-invariant function f , $f(\mathbf{p}) = f(-\mathbf{p})$, to which we shall restrict ourselves in the following, no partial integration is needed and, moreover, the two terms in the current (5) are covariantly conserved individually: Using (2) we have

$$D \cdot j \propto \int \frac{d^3 p}{(2\pi)^3} (\tilde{f}_1 F^{0\gamma} v_\gamma + \tilde{f}_2 F^{z\gamma} v_\gamma) = 0 \quad (6)$$

where parity invariance of f_1 makes the \mathbf{v} in the first term integrate to zero. In the second term f_2 is odd with respect to the z -direction, so that only the term involving $F^{zz} v_z$ could contribute, but $F^{zz} \equiv 0$.

The dynamical system described by Eqs. (1)–(3) has constant total energy of the form

$$\mathcal{E} = \int d^3 x \operatorname{tr} (\mathbf{E}^2 + \mathbf{B}^2)|_t + \int_{t_0}^t dt' \int d^3 x 2 \operatorname{tr} \mathbf{j}_{t'} \cdot \mathbf{E}_{t'}. \quad (7)$$

The part containing the induced current involves

$$\begin{aligned} \operatorname{tr} \mathbf{j} \cdot \mathbf{E} &= \frac{g^2}{4} \partial_\mu \int \frac{d^3 p}{(2\pi)^3} \tilde{f}_1 v^\mu W_0^2 \\ &\quad + \frac{g^2}{2} \int \frac{d^3 p}{(2\pi)^3} \tilde{f}_2 W^z (v \cdot D) W_0, \end{aligned} \quad (8)$$

which shows that in the isotropic case ($\tilde{f}_2 = 0$) there is a local, positive definite energy contribution from the plasma [29]. However, in the general anisotropic case, positivity is lost. This reflects the possibility of plasma instabilities, where energy may be extracted from hard particles and deposited into the soft collective fields without bound as long as the hard-loop approximation $A_\mu \ll |\mathbf{p}|/g$ remains valid.

III. DISCRETIZED HARD LOOPS

The structure of Eqs. (1)–(3) is such that only W_0 and W_z participate nontrivially in the dynamical evolution. A closed set of gauge-covariant equations is thus obtained when the hard-loop integral in (5) is discretized with respect to directions \mathbf{v}

$$\begin{aligned} j^\mu(x) &= g^2 \int \frac{p^2 dp}{(2\pi)^2} \frac{1}{\mathcal{N}} \sum_{\mathbf{v}} v^\mu [\tilde{f}_1 W_{\mathbf{v}}^0(x) + \tilde{f}_2 W_{\mathbf{v}}^z(x)] \\ &\equiv \frac{1}{\mathcal{N}} \sum_{\mathbf{v}} v^\mu [a_{\mathbf{v}} W_{\mathbf{v}}^0(x) + b_{\mathbf{v}} W_{\mathbf{v}}^z(x)], \end{aligned} \quad (9)$$

where the \mathcal{N} unit vectors \mathbf{v} define a partition of the unit sphere in patches of equal area. The coefficients $a_{\mathbf{v}}$, $b_{\mathbf{v}}$ are constants defined by

$$a_{\mathbf{v}} = -g^2 \int_0^\infty \frac{p^2 dp}{(2\pi)^2} f_1(|\mathbf{p}|, |\mathbf{p}|v^z), \quad (10)$$

$$b_{\mathbf{v}} = -g^2 \int_0^\infty \frac{p^2 dp}{(2\pi)^2} f_2(|\mathbf{p}|, |\mathbf{p}|v^z). \quad (11)$$

Isotropic distribution functions f are characterized by $a_{\mathbf{v}}$'s which are independent of \mathbf{v} , and vanishing $b_{\mathbf{v}}$'s.

The special choice of Ref. [11, 12] for an anisotropic distribution function,

$$\tilde{f}(|\mathbf{p}|, p^z) = N(\xi) f_{iso}(\mathbf{p}^2 + \xi p_z^2), \quad (12)$$

gives

$$a_{\mathbf{v}} = \frac{N(\xi) m_D^2}{(1 + \xi v_z^2)^2}, \quad b_{\mathbf{v}} = \xi v_z a_{\mathbf{v}}, \quad (13)$$

where m_D is the Debye mass of the isotropic case $\xi = 0$. If one requires that the number density of hard particles is the same for different values ξ , the normalization factor here is $N(\xi) = \sqrt{1 + \xi}$. In the following we shall often use the abbreviation

$$m^2 \equiv N(\xi) m_D^2, \quad (14)$$

leaving open the possibility for different normalizations.³

Discretization of the directions \mathbf{v} can spoil the reflection properties of $f_{1,2}$ and thus automatic covariant conservation of j by virtue of Eq. (6). Covariant current conservation is however guaranteed when $a_{\mathbf{v}}$, $b_{\mathbf{v}}$ satisfy

$$\sum_{\mathbf{v}} a_{\mathbf{v}} \mathbf{v} = 0, \quad \sum_{\mathbf{v}} b_{\mathbf{v}} = 0, \quad \sum_{\mathbf{v}} b_{\mathbf{v}} \mathbf{v}_{\perp} = 0, \quad (15)$$

where $\mathbf{v}_{\perp} = \mathbf{v} - v^z \mathbf{e}_z$, and so we shall restrict ourselves to discretizations of this kind.

A suitable discretization of the sphere is given by a set of unit vectors \mathbf{v} following from regular spacing in z and φ according to

$$z_i = -1 + (2i - 1)/N_z, \quad i = 1 \dots N_z, \quad \varphi_j = 2\pi j/N_{\varphi}, \quad j = 1 \dots N_{\varphi}. \quad (16)$$

The resulting “disco balls” are such that they are covered with $\mathcal{N} = N_z \times N_{\varphi}$ (curved) tiles of equal area. For low values of \mathcal{N} , we shall also consider discretized \mathbf{v} 's pointing to the centers of the faces of one of the regular polyhedra with $\mathcal{N} = 6, 8, 12$ or 20.

Given any set of \mathbf{v} , $a_{\mathbf{v}}$, $b_{\mathbf{v}}$, satisfying (15), one has then to solve (9) together with the Yang-Mills field equations and

$$[v \cdot D(A)] W_{\beta}^{\mathbf{v}}(x) = F_{\beta\gamma}(A) v^{\gamma}, \quad \beta = 0, 3. \quad (17)$$

In temporal axial gauge $A^0 = 0$, the dynamical variables are A_i , $E_i = -\dot{A}_i$, $W_0^{\mathbf{v}}$ and $W_z^{\mathbf{v}}$. Eq. (17) becomes

$$\partial_t W_{\beta}^{\mathbf{v}}(x) = -\mathbf{v} \cdot \mathbf{D} W_{\beta}^{\mathbf{v}} + F_{\beta\gamma}(A) v^{\gamma}. \quad (18)$$

The gauge choice $A^0 = 0$ is in fact merely a convenience for the following numerical simulations. All equations are gauge covariant, the current is covariantly conserved, and we shall also consider exclusively gauge invariant observables in our numerical simulations.

Through Eq. (9) only a linear combination of $W_{\mathbf{v}}^0$ and $W_{\mathbf{v}}^z$ participates actively in the dynamical evolution. So in addition to the gauge fields we need to consider only the \mathcal{N} auxiliary fields

$$\mathcal{W}_{\mathbf{v}}(x) = a_{\mathbf{v}} W_{\mathbf{v}}^0(x) + b_{\mathbf{v}} W_{\mathbf{v}}^z(x). \quad (19)$$

³ Note that Ref. [11] has $N(\xi) = 1$.

The full hard-loop dynamics is then approximated by the following set of matrix-valued equations,

$$[v \cdot D(A)]\mathcal{W}_{\mathbf{v}} = (a_{\mathbf{v}}F^{0\mu} + b_{\mathbf{v}}F^{z\mu})v_{\mu} \quad (20)$$

$$D_{\mu}(A)F^{\mu\nu} = j^{\nu} = \frac{1}{\mathcal{N}} \sum_{\mathbf{v}} v^{\nu} \mathcal{W}_{\mathbf{v}}, \quad (21)$$

which can be systematically improved by increasing \mathcal{N} .

The Gauss law constraint is explicitly

$$D_i(A)F^{i0} = -D_i(A)\dot{A}^i = j^0 = \frac{1}{\mathcal{N}} \sum_{\mathbf{v}} \mathcal{W}_{\mathbf{v}}. \quad (22)$$

In the case of an isotropic plasma, a similar discretization of the hard-loop dynamics which uses a discrete set of vectors \mathbf{v} has been considered before by Rajantie and Hindmarsh [30]. A different possibility for discretization that has been employed previously is a decomposition of the auxiliary fields $W^{\mu}(x; v)$ into spherical harmonics [30, 31] and truncating at a maximal angular momentum l_{max} . This method has now also been used in the most recent numerical study of non-Abelian plasma instabilities by Arnold et al. [26]. Discretizing \mathbf{v} is slightly simpler, but also more flexible in that it allows one to e.g. improve approximations in highly anisotropic cases with cylindrical symmetry by selectively increasing the resolution in the z direction more than in the φ direction.

When the momentum space distribution of hard modes has an oblate form, $\xi > 0$ in Eq. (12), the momenta of the unstable collective modes form prolate regions with $|k_z| > 0$ [11, 21]. For a given k_z , the growth rate is largest for $k_{\perp} = 0$, i.e. the constant modes with respect to the directions transverse to the direction of momentum space anisotropy. By considering initial conditions which are constant in the transverse direction, we can study the complete dynamics of these particular unstable modes in a 1+1-dimensional setting where all fields are dimensionally reduced, $(x) \rightarrow (t, z)$. Then only $A_z(t, z)$ plays the role of a gauge field, and $A_{x,y}(t, z)$ behave as adjoint matter.

Using temporal axial gauge, the equations of motion for the dynamical fields can then be simplified according to

$$\begin{aligned} \partial_t^2 A_x &= D_z^2 A_x - g^2[A_y, [A_y, A_x]] + j^x \\ \partial_t^2 A_y &= D_z^2 A_y - g^2[A_x, [A_x, A_y]] + j^y \\ \partial_t^2 A_z &= -ig[A_x, D_z A_x] - ig[A_y, D_z A_y] + j^z \\ (\partial_t + \mathbf{v} \cdot \mathbf{D})\mathcal{W}_{\mathbf{v}} &= a_{\mathbf{v}}(-\mathbf{v} \cdot \partial_t \mathbf{A}) + b_{\mathbf{v}}[-\partial_t A_z + D_z(v_x A_x + v_y A_y)], \end{aligned} \quad (23)$$

where $\mathbf{D} = \nabla + ig[\mathbf{A}, \cdot]$, $\nabla = (0, 0, \partial_z)$, and $\mathbf{j} = \frac{1}{\mathcal{N}} \sum_{\mathbf{v}} \mathbf{v} \mathcal{W}_{\mathbf{v}}$.

In Sect. VI we shall also consider initial conditions which are not constant with respect to the transverse directions. This will then require the full 3+1-dimensional content of Eqs. (20) and (21).

IV. COMPARISON OF DISPERSION LAWS

Before turning to the numerical evaluation of the above equations by also discretizing space and time, we shall study the dispersion laws of linearized modes, and the consequences

of replacing the continuous set of fields $W^\beta(x, \mathbf{v})$ by a finite number $W_\mathbf{v}^\beta(x)$. Because we shall be interested mainly in the unstable modes, we shall concentrate on wave-vectors parallel to the anisotropy axis, which includes the most unstable modes. With $k^i = k\delta_z^i$, there are then only two possible modes for gauge fields, transverse and longitudinal ones [11, 12].

A. Continuum results

For anisotropic distribution functions (12), analytical results for the gluonic self-energies have been obtained in Ref. [11, 12], which we recapitulate for the special case of longitudinal wave vectors.

1. Transverse polarizations

With $\eta = \omega/k$, the transverse gluon self-energy reads [12]

$$\begin{aligned} \Pi_t = \frac{m^2}{4\sqrt{\xi}(1+\xi\eta^2)^2} & \left[(1+\eta^2+\xi(-1+(6+\xi)\eta^2-(1-\xi)\eta^4)) \arctan \sqrt{\xi} \right. \\ & \left. + \sqrt{\xi}(\eta^2-1) \left(1+\xi\eta^2-(1+\xi)\eta \ln \frac{\eta+1+i\epsilon}{\eta-1+i\epsilon} \right) \right], \end{aligned} \quad (24)$$

where we recall that $m^2 = N(\xi)m_D^2(\xi=0)$.

The limit $k \rightarrow 0$ or $\eta \rightarrow \infty$ determines the transverse plasma frequency as⁴

$$\omega_{pl,t}^2 = \frac{1}{4\xi} \left(1 + \frac{\xi-1}{\sqrt{\xi}} \arctan \sqrt{\xi} \right) m^2. \quad (25)$$

For large momenta, the transverse excitations tend to the asymptotic mass given by

$$m_\infty^2/m^2 = \frac{1}{2\sqrt{\xi}} \arctan \sqrt{\xi}. \quad (26)$$

The static limit on the other hand gives a mass squared which is determined by the relation

$$m_m^2 \equiv -\mu^2 = -\xi\omega_{pl,t}^2. \quad (27)$$

For negative ξ , this indicates screening of magnetostatic fields, while for positive ξ there is an instability for all momenta $k < \mu$.

2. Longitudinal polarizations

In the longitudinal sector we have [12]

$$\begin{aligned} \Pi_\ell = -\frac{\eta^2 m^2}{2\sqrt{\xi}(1+\xi\eta^2)^2} & \left[(1+\xi)(1-\xi\eta^2) \arctan \sqrt{\xi} \right. \\ & \left. + \sqrt{\xi} \left((1+\xi\eta^2) - (1+\xi)\eta \ln \frac{\eta+1+i\epsilon}{\eta-1+i\epsilon} \right) \right]. \end{aligned} \quad (28)$$

⁴ For $-1 < \xi < 0$ one has to replace $\frac{1}{\sqrt{\xi}} \arctan \sqrt{\xi}$ by $\frac{1}{\sqrt{-\xi}} \operatorname{artanh} \sqrt{-\xi}$.

The plasma frequency in the longitudinal sector is generally different from the one in the transverse sector when $\xi \neq 0$ and reads

$$\omega_{pl,\ell}^2 = \frac{1}{2\xi} \left(\frac{1+\xi}{\sqrt{\xi}} \arctan \sqrt{\xi} - 1 \right) m^2. \quad (29)$$

The static limit of Π_ℓ/η^2 gives the electric screening mass squared

$$m_{el}^2 = \frac{1}{2} \left(\frac{1+\xi}{\sqrt{\xi}} \arctan \sqrt{\xi} + 1 \right) m^2 = m^2 + \xi \omega_{pl,\ell}^2. \quad (30)$$

This parameter does not change sign for all $-1 \leq \xi < \infty$, so in the present case of wave vectors parallel to the anisotropy direction all instabilities are purely transverse.

B. v-discretized hard loops

After discretizing the space of velocities and approximating the fields $W^\beta(x, \mathbf{v})$ by a finite set of field $W_\mathbf{v}^\beta(x)$, we search for solutions of Eqs. (23) where all fields point in a fixed color direction and which correspond to a single Fourier mode in z -direction:

$$A^i(t, z) = e^{\gamma t} e^{ikz} \epsilon^i, \quad W_\mathbf{v}^{0,z}(t, z) = e^{\gamma t} e^{ikz} w_\mathbf{v}^{0,z}. \quad (31)$$

Here k will usually be a real number, while γ can be either real or imaginary, corresponding to exponential or oscillatory behavior, respectively. The dynamics is then effectively Abelian and linearized, and Eqs. (23) reduce to

$$\gamma^2 \epsilon^i + k^2 \epsilon_\perp^i = \frac{1}{\mathcal{N}} \sum_{\mathbf{v}} v^i (a_\mathbf{v} w_\mathbf{v}^0 + b_\mathbf{v} w_\mathbf{v}^z) \quad (32)$$

$$(\gamma + ikv_z) w_\mathbf{v}^0 = -\gamma v^i \epsilon^i \quad (33)$$

$$(\gamma + ikv_z) w_\mathbf{v}^z = -\gamma \epsilon^z + ikv^i \epsilon_\perp^i \quad (34)$$

with $\epsilon_\perp^i = (\epsilon^x, \epsilon^y, 0)$. The Gauss law constraint reads

$$-ik\gamma \epsilon^z = \frac{1}{\mathcal{N}} \sum_{\mathbf{v}} (a_\mathbf{v} w_\mathbf{v}^0 + b_\mathbf{v} w_\mathbf{v}^z). \quad (35)$$

Next we specialize to the anisotropic distribution function (12), for which the coefficients $a_\mathbf{v}$, $b_\mathbf{v}$ are given by (13), and compare with the above continuum results. With discretized \mathbf{v} 's we obtain algebraic equations that can be solved in closed form for the regular polyhedra with $\mathcal{N} = 6, 8, 12, 20$. Taking the \mathbf{v} 's to point to the centers of the faces of these polyhedra, we consider two different orientations for each polyhedron: one where the discrete rotational symmetry around the z -axis is maximal, and one where this symmetry is only Z_3 . The two choices sample in particular different sets of z -components of hard momenta (in Table II in Appendix A 2 the number of distinct z -components is indicated by N_z). We shall also work out the dispersion laws in a few cases of larger \mathcal{N} using Eqs. (16).

1. Transverse polarizations

Equations (32) give algebraic relations between γ and k , while the Gauss law constraint is automatically fulfilled for reflection-symmetric distribution functions, which lead to the restrictions (15).

For the cube ($\mathcal{N} = 6$) and Z_4 symmetry about the z -axis, the solution is simply

$$\gamma^2 = -\omega^2 = -(k^2 + m^2/3), \quad (36)$$

corresponding to a propagating mode with momentum-independent mass equal to the isotropic plasma frequency. In this case, the ξ -dependence drops out completely (except for a possible normalization of m according to (14)). The result (36) is in fact identical to the one obtained by discretization through spherical harmonics and truncating at angular momentum $l_{max} = 1$ [31].

For $\mathcal{N} = 6$ and Z_3 symmetry about the z -axis, the solution is more complicated, and happens to coincide with the $\mathcal{N} = 8$, Z_4 case. These two cases give the biquadratic equation

$$\gamma^2 + k^2 = \underbrace{\frac{m^2}{(1 + \xi/3)^2}}_a \frac{-\gamma^2 + \xi k^2/3}{3\gamma^2 + k^2}. \quad (37)$$

This equation obviously has solutions for real γ (i.e. instabilities) only when $\xi > 0$, as is the case for the continuum solutions. There are two branches of solutions given by

$$\gamma^2 \equiv -\omega^2 = -\frac{1}{6} \left[a + 4k^2 \pm \sqrt{a^2 + (8 + 4\xi)ak^2 + 4k^4} \right] \quad (38)$$

The upper sign corresponds to propagating transverse plasmons. As can be seen from Table II in Appendix A 2, there is considerable improvement compared to the simple dispersion law (36) of the $\mathcal{N} = 6$, Z_4 case — the asymptotic mass and its small- ξ correction are even exact. The lower sign in (38) contains the instability for $\xi > 0$, and oscillatory behavior for $k > \mu$. Fig. 1a shows a plot of the solutions of (38) and compares it with the continuum result following from (24).

The $\mathcal{N} = 8$, Z_3 case and the $\mathcal{N} = 12$, Z_5 case also lead to biquadratic equations, each with somewhat different coefficients, and the small- ξ behavior can be read from Table II.

The $\mathcal{N} = 12$, Z_3 case and the icosahedron, $\mathcal{N} = 20$, on the other hand, lead to bicubic equations, with $\mathcal{N} = 12$, Z_3 and $\mathcal{N} = 20$, Z_5 sharing the same equation⁵, namely

$$\gamma^2 + k^2 = -15m^2 \frac{(45\gamma^4 - k^4\xi)(45 + 42\xi + 13\xi^2) + 3\gamma^2k^2(315 + 255\xi + 93\xi^2 - 7\xi^3)}{(45 + 30\xi + \xi^2)^2(45\gamma^4 + 30\gamma^2k^2 + k^4)}. \quad (39)$$

The case $\mathcal{N} = 20$, Z_3 gives a similar equation but with different coefficients. The solutions to these equations can be given in closed form, but are too unwieldy to be reproduced here. There are now three distinct solutions one of which corresponds to propagating transverse plasmons.

⁵ As is well known, the regular polyhedra $\mathcal{N} = 6, 8$ and $\mathcal{N} = 12, 20$ form dual pairs, however this does not seem to explain the coincidence of the dispersion laws of $\mathcal{N} = 6$, Z_3 with $\mathcal{N} = 8$, Z_4 and of $\mathcal{N} = 12$, Z_3 with $\mathcal{N} = 20$, Z_5 , since duality would map orientations with rotational symmetry Z_3 to such with Z_3 .

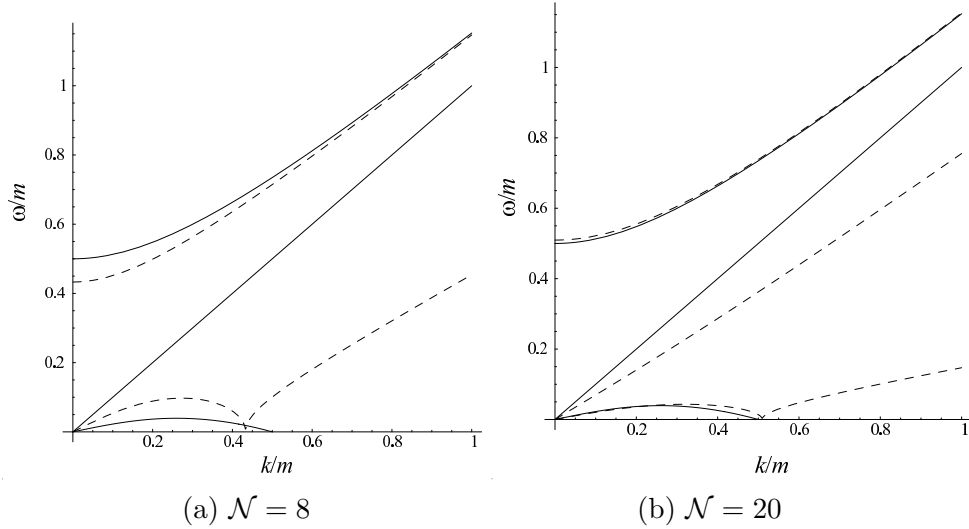


FIG. 1: The transverse dispersion laws $\omega(k)$ for anisotropy parameter $\xi = 1$ in the continuum (full lines) compared with those of \mathbf{v} -discretized hard loops for the octahedron ($\mathcal{N} = 8$, Z_4) and the icosahedron ($\mathcal{N} = 20$, Z_5) (dashed lines). The unstable modes appear at small space-like momenta where the plot is in terms of $\gamma(k)$ instead of $\omega(k)$. The additional space-like modes are approximations of the Landau cut by simple poles whose number increases with \mathcal{N} .

Except for the cube with Z_4 symmetry, Eq. (36), there is always exactly one solution which contains an instability for $\xi > 0$ and $k < \mu$. A significant difference to the continuum result is however the absence of Landau damping. Instead, there are additional modes for spacelike momenta, and their number increases with \mathcal{N} , approximating the logarithmic cut by more and more poles at spacelike momenta. This is analogous to what has been observed in Ref. [31] for discretizations using spherical harmonics. However, in the anisotropic case, one of these spacelike modes becomes unstable for $\xi > 0$. In the continuum limit, the unstable part ($k \leq \mu$) remains on the physical sheet, whereas its stable, oscillatory part moves to the unphysical sheet, cf. Ref. [12].

In Fig. 1b we show the transverse dispersion laws for $\xi = 1$ following from (39), which has two spacelike branches. The comparison with the continuum case shows that both the timelike propagating modes and the instabilities are quite well reproduced quantitatively.

Our main interest will clearly be the plasma instabilities. Since all the actual and additional stable modes are just oscillatory, we do not expect them to play an important role in the evolution of the instabilities. For us the most important aspect of the dispersion laws will be the magnitude of $\gamma(k)$ for the unstable modes $k \leq \mu$. The continuum result for $\gamma(k)$ has the property that it vanishes both at $k = 0$ and at $k = \mu$, in contrast with the toy model studied in Ref. [24]. This feature is correctly reproduced in our discretization of the hard-loop dynamics of anisotropic plasmas. In Figs. 2 we compare $\gamma(k)$ of the various polyhedra (with maximal Z_φ) with the exact continuum result for some values of ξ . From this we expect that all the polyhedral approximations should be qualitatively correct, with $\mathcal{N} = 20$ being a quantitatively good approximation for $\xi \lesssim 10$.

For higher \mathcal{N} we use the “disco-ball” discretization (16). Fig. 3 compares the growth rates $\gamma(k)$ for full and discretized hard loops with $\mathcal{N} = \mathcal{N}_z \times \mathcal{N}_\varphi = 20 \times 5 = 100$ and $\xi = 10$, which shows that the latter give very accurate approximations for $\mathcal{N} \gtrsim 100$. Also the dispersion laws of propagating stable modes are accurately reproduced. For example,

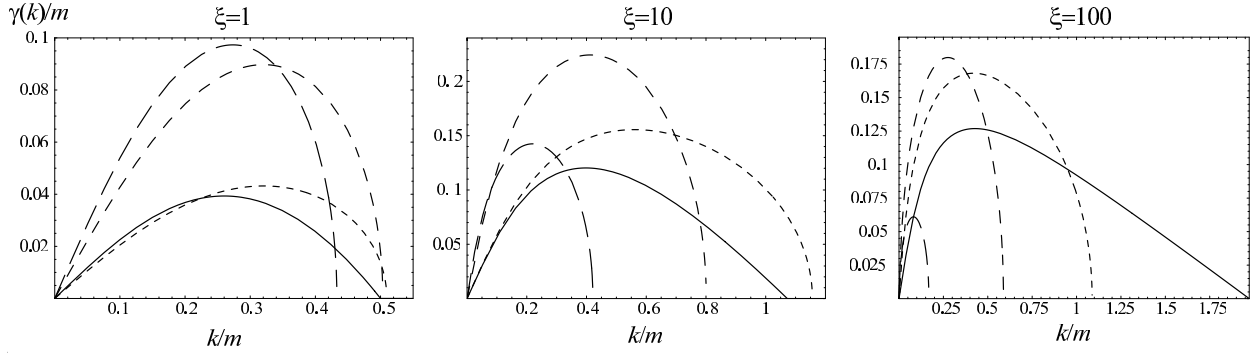


FIG. 2: The growth rate $\gamma(k)$ of unstable modes for the polyhedral approximations $\mathcal{N} = 8, 12, 20$ and maximal Z_φ (dashed lines with smaller and smaller dashes) in comparison with the continuum result (black lines) for $\xi = 1, 10$, and 100 .

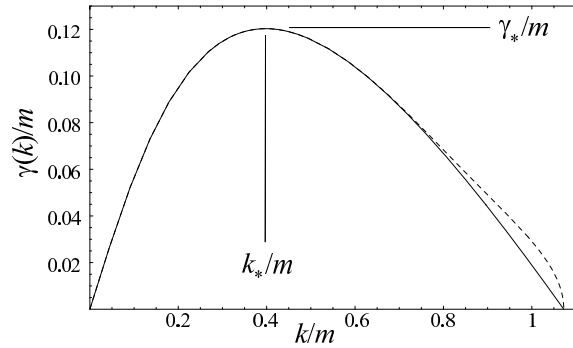


FIG. 3: The growth rate $\gamma(k)$ of unstable modes for the discretized hard loops with $\mathcal{N} = 100$ (dashed line) in comparison with the continuum result (solid line) for $\xi = 10$. The precise values of wave number k_* and growth rate γ_* corresponding to the mode of maximal growth can be read from Table I.

with $\xi = 10$, $\mathcal{N} = 100$, the continuum result for the asymptotic mass (A3) of the transverse modes with $|\mathbf{k}| \gg \mu$ is reproduced with an error of only 0.017%

In the following numerical simulations, we shall employ the disco-ball discretization with $\mathcal{N} \geq 100$, choosing $N_z \gg N_\varphi$ to take into account that the distribution function varies more rapidly in the z than in the φ -direction. When considering smaller \mathcal{N} , we shall instead take regular polyhedra, which as discussed further in Appendix A 2, seem to be superior approximations for $\mathcal{N} \leq 20$. Before turning to these numerical simulations, we complete this section by briefly considering also the (stable) longitudinal modes.

2. Longitudinal polarizations

For longitudinal polarizations ($\epsilon^z \neq 0$) the Gauss law constraint (35) is nontrivial, but it leads to the same equation as the linearized field equation (32). For the regular polyhedra, the resulting algebraic relations between γ and k can be solved in closed form, and one finds that as expected there are only stable solutions $-\gamma^2 = \omega^2 \geq 0$.

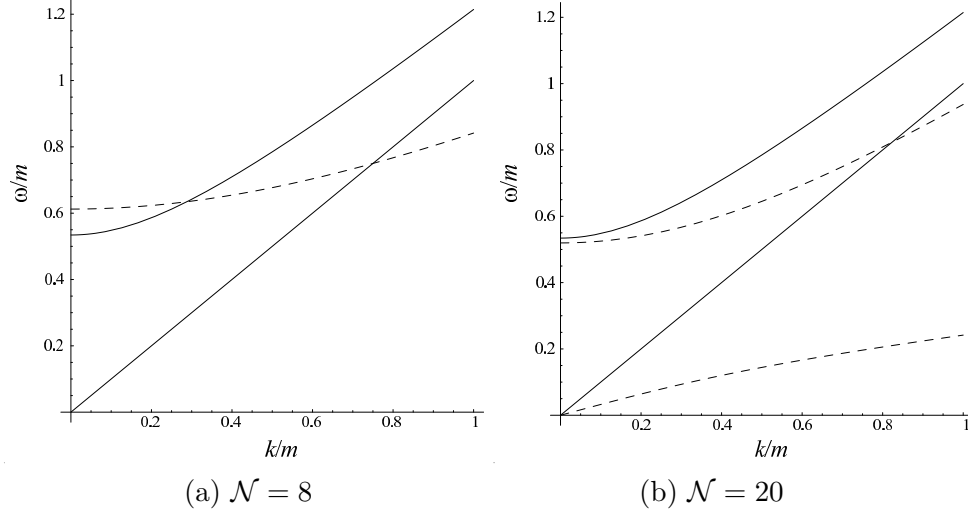


FIG. 4: The longitudinal dispersion laws $\omega(k)$ for $\xi = 1$ in the continuum (full lines) and for the octahedron ($\mathcal{N} = 8$, Z_4) and the icosahedron ($\mathcal{N} = 20$, Z_5) (dashed lines).

For $\mathcal{N} = 6$ and Z_4 symmetry about the z -axis, the solution is

$$\omega^2 = \frac{m^2}{3(1+\xi)} + k^2, \quad (40)$$

corresponding to a propagating mode with momentum-independent mass which at $\xi = 0$ equals the correct plasma frequency. In the static limit, the Debye mass is off by a factor $1/\sqrt{3}$.

The cases $\mathcal{N} = 6$ with Z_3 symmetry about the z -axis and $\mathcal{N} = 8$ with Z_4 symmetry have a similarly simple solution, which however reproduces both the plasma frequency and the Debye mass in the isotropic limit through the dispersion law

$$\omega^2 = \frac{m^2(1+\xi)}{3(1+\xi/3)^2} + \frac{k^2}{3}. \quad (41)$$

At larger momenta the solution becomes spacelike, whereas the continuum dispersion law would approach the light-cone exponentially in the timelike domain.

With increasing \mathcal{N} , the continuum result for the longitudinal dispersion relations is approximated from below (i.e. spacelike momenta) by the mode with largest frequency. The Landau cut at spacelike momenta is approximated by an increasing number of poles, one of which is connected to the time-like plasmon mode.⁶ For $\mathcal{N} = 12$ and 20, there are again two spacelike branches, now given by biquadratic equations. The cases $\mathcal{N} = 20$, Z_5 and $\mathcal{N} = 12$, Z_3 again share the same equation, which reads

$$45\omega^4 - 30\omega^2 k^2 + k^4 = \frac{135m^2(1+\xi)}{45+30\xi+\xi^2} [5\omega^2(45+6\xi+\xi^2) - k^2(15+10\xi+3\xi^2)]. \quad (42)$$

⁶ In the continuum, the longitudinal plasmons have effectively a finite range of possible momenta because the residue vanishes exponentially as the light-cone is approached.

V. 1+1-DIMENSIONAL LATTICE SIMULATIONS

In the previous section we have seen that for oblate momentum distributions of plasma constituents, $\xi > 0$, there are unstable modes for $|k_z| < \mu$ and sufficiently small k_\perp . In the linear regime, where field amplitudes A are much smaller than k/g , time evolution is determined by the above dispersion laws and all modes evolve independently. Unstable modes grow exponentially with growth rate $\gamma(\mathbf{k})$, which for a given value of k_z is largest when $k_\perp = 0$. We denote the scale of maximal growth by k_* and the corresponding maximal growth rate by γ_* . This scale is of the same order of magnitude as the Debye screening mass or the thermal mass of propagating plasmons, namely $\sim gp_{hard}$, which at weak coupling is much larger than the color relaxation scale $\sim g^2 p_{hard}$ or the scale of large-angle scattering rates $\sim g^4 p_{hard}$. This is what makes plasma instabilities a prime candidate for the mechanism of fast isotropization in a weakly coupled plasma.

In the following we shall study the evolution of collective soft fields starting from tiny random fluctuations. If the initial field amplitudes are sufficiently small to give a large number of e-folds in the linear regime, this will lead to field configurations that are dominated by the modes of largest growth. For $\xi > 0$ this will favor modes with $|k_z| \approx k_*$ and $k_\perp \approx 0$. The special initial conditions with strictly $k_\perp = 0$, i.e. constant modes with respect to the spatial directions transverse to the anisotropy direction should therefore be an idealization of particular interest. All fields are then functions of only one spatial coordinate, and the equations of motion are simplified according to Eqs. (23).

In Ref. [24], non-Abelian dynamics with such initial conditions was studied numerically with a drastically simplified model for the induced current (1), namely

$$j_\alpha^{AL} = \mu^2 A_\alpha, \quad \alpha = x, y. \quad (43)$$

As was shown in Ref. [24], this correctly reflects the static limit of the anisotropic hard-loop effective action for fields that vary only in the anisotropy direction, but it neglects its general frequency dependence and dynamical nonlinearity. Already at the linearized level, the former complication means that modes with vanishing wave vector, $\mathbf{k} = 0$, are stable, see Figs. 2 and 3, whereas the toy model (43) implies a growth rate $\gamma = \sqrt{\mu^2 - \mathbf{k}^2}$, which is maximal at $\mathbf{k} = 0$, where it equals μ . As Figs. 2 and 3 show, the anisotropic distribution function (12) with $\xi > 0$ leads to $\gamma_* < k_* < \mu$ instead.

In simulations of the toy model (43), the authors of Ref. [24] have found that unstable non-Abelian modes, which are constant modes with respect to transverse space, might behave very similarly to Abelian Weibel instabilities also in the nonlinear regime. In the latter, they observed rapid Abelianization, both locally and globally.

Using the \mathbf{v} -discretized equations of motion, (20) and (21), we have extended the lattice simulations of Ref. [24] to the full hard-loop effective theory, with the main findings presented in Ref. [25]. In the 1+1-dimensional situation we found some modification of the evolution of the instabilities when they first reach nonlinear size. Subsequently, growth with rates close to the Abelian growth rate was restored, however.

In the most recent paper [26] a similar analysis was performed, using a different discretization method for the hard-loop effective theory. While confirming our 1+1-dimensional findings, they also considered random initial fluctuations in all spatial directions and the resulting 3+1-dimensional evolution with the conclusion that the late-time behavior, deeper in the nonlinear regime, is in fact modified importantly. In this section we shall concentrate on the 1+1-dimensional situation, giving a detailed account of the results presented in

TABLE I: Debye mass m_{el} , magnetic instability scale μ , wave vector k_* and growth rate γ_* for the modes of maximal growth, transverse and longitudinal plasma frequency, and the asymptotic mass of transverse gluons for the isotropic case and the anisotropic case assumed in the numerical simulations.

ξ	m_{el}/m	μ/m	k_*/m	γ_*/m	$\omega_{pl,t}/m$	$\omega_{pl,\ell}/m$	m_∞/m
0	1	–	–	–	0.577350	0.577350	0.707107
10	1.64296	1.07225	0.398025	0.120289	0.339075	0.412228	0.447144

Ref. [25]. After extending this also to gauge group $SU(3)$, we shall give our first results for a 3+1-dimensional simulation of the \mathbf{v} -discretized hard-loop effective equations in Sect. VI.

Like Ref. [24] we work in temporal axial gauge, $A^0 = 0$, and take initial conditions corresponding to small random chromoelectric fields $\mathbf{E} = -\partial_t \mathbf{A}$ with polarization transverse to the z -axis, and all other fields vanishing, which in our case includes the auxiliary fields $\mathcal{W}_{\mathbf{v}}$. This initial condition satisfies the Gauss law constraint, $\mathbf{D} \cdot \mathbf{E} = \mathcal{N}^{-1} \sum_{\mathbf{v}} \mathcal{W}_{\mathbf{v}}$, whose continued fulfilment is monitored in the simulation, but not enforced. As a further non-trivial check of our numerics, we tracked conservation of the total energy (7), stopping the simulation when this signalled loss of accuracy. The lattice versions of the 1+1 dimensional equations of motion that we have employed are given in detail in Appendix B.

In the 1+1-dimensional simulations below we used anisotropy parameter $\xi = 10$. We shall express all dimensionful quantities by the asymptotic mass of transverse excitations, whose relation to the mass scale m appearing in the coefficients (13) is given in Table I. While the coupling constant g could be absorbed by redefinitions of our dynamical quantities, we shall make their appearance explicit in our final results.

The lattice spacing used in the simulations presented in this section was chosen such that $a = 0.0707 m_\infty^{-1}$. We have taken a one-dimensional spatial lattice with periodic boundary conditions and 5,000 sites, so that the physical size is $L \approx 350 m_\infty^{-1}$. We shall show results for the icosahedron $\mathcal{N} = 20$, Z_5 , and disco-ball discretizations $\mathcal{N} = 100, 800$, and 2000, with $N_z \times N_\varphi = 20 \times 5, 50 \times 16$, and 100×20 , respectively. In the leapfrog algorithm specified in Appendix B we used time steps ϵ/a from 1/100 to 1/250. The initial conditions are given in Eq. (B10), and the choice of the parameter σ therein corresponds to starting with a random initial seed chromoelectric field of root-mean-square amplitude $0.012 m_\infty^2/g$.

In the numerical simulations, the Gauss law constraint, which is satisfied by the initial conditions, remained satisfied within machine accuracy throughout. As a further check, we monitored the total energy (7) and stopped the simulation when this had $O(1)$ violations. For all but the largest times, this quantity was conserved within less than 1%; only at the very end when the energy in the various field components had grown by factors larger than 10^6 was there energy violation at the percentage level, which quickly thereafter exploded, signalling uncontrollable discretization errors.

A. Currents and energies

Fig. 5 shows the evolution of the average root-mean-square transverse and longitudinal currents and charge density defined by

$$j_{rms}^{\perp,z,0} = \left[\int_0^L \frac{dz}{L} 2 \text{tr} ((\mathbf{j}^{\perp,z,0})^2) \right]^{1/2}, \quad (44)$$

comparing the cases $\mathcal{N} = 100, 800$, and 2000 . The transverse current grows exponentially with a growth rate that is most of the time only slightly below γ_* , except for a transitory reduction at the beginning of the nonlinear regime, when $j_{rms} \sim m_\infty^3/g$. Our initial condition (only nonvanishing transverse electric fields at $t = 0$) give rise to longitudinal currents and charge densities only through non-Abelian interactions (in the Abelian regime all modes would decouple and evolve independently according to the linearized dispersion laws). The non-Abelian interactions naturally lead to growth rates for j^z and j^0 which are double that of j^\perp , and such a behavior is seen in Fig. 5 after some initial delay caused by the fact that the unstable modes first have to grow out of the initial random mixture of stable and unstable ones. The different cases $\mathcal{N} = 100, 800$, and 2000 lead to only slightly different behavior in the nonlinear regime, where higher \mathcal{N} seems to be required to capture the precise variations of the subdominant components j^z and j^0 .

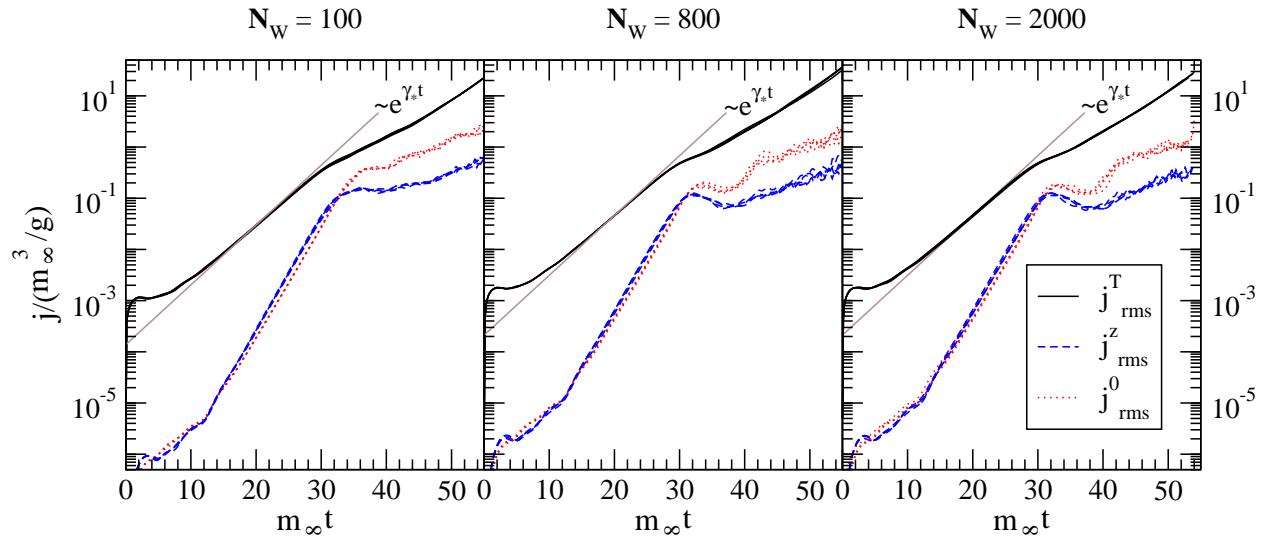


FIG. 5: The average current j_{rms}^\perp (black), j_{rms}^z (blue) and rms charge density j_{rms}^0 (red) for $N_W \equiv \mathcal{N} = 100, 800, 2000$ using a collection of 4 runs each with different random initial conditions.

Closely related to this, Fig. 6 shows how the exponentially growing energy that is transferred from hard to soft scales gets distributed among chromomagnetic and chromoelectric collective fields. The dominant contribution is in transverse magnetic fields, and it grows roughly with the maximum rate γ_* both in the linear as well as in the highly nonlinear regime, with a transitory slowdown in between. Transverse electric fields behave similarly, and are suppressed by a factor of the order of $(\gamma_*/k_*)^2$. Notice that in the model of Ref. [24]

the situation would be different: Because k_* is zero there, the dominant energy component is then from transverse electric fields, whereas the relative importance of magnetic fields drops with time. In the 1+1-dimensional evolution, the transverse magnetic field component is the dominant one, both in the linear and in the nonlinear regime.

The appearance of longitudinal contributions, which are absent in the initial conditions we have chosen, is again a purely non-Abelian effect. While completely negligible at first, they have a growth rate which is double the one in the transverse sector, and they begin to catch up with the latter when the nonlinear regime is reached first. At this point, the general growth stalls for a time of order γ_*^{-1} . When the transverse magnetic field resumes its growth (with the transverse electric field following with some delay), the respective longitudinal components drop for some time before also starting to grow again. This dip in the subdominant longitudinal components turns out to depend on \mathcal{N} , whereas the overall behavior is already reproduced well by the rather small value of $\mathcal{N} = 20$ (the icosahedron).

Deeper into the nonlinear regime, the (transversely constant) unstable modes grow at roughly equal rates. There the results are only weakly dependent on the degree of hard-loop discretization, \mathcal{N} .

B. Color correlation

Had we assumed initial conditions where all fields would point in the same color direction all over the spatial lattice, we would have found only strictly exponential growth once the stable modes have become of negligible importance. The behavior would then be exactly the same as with Abelian Weibel instabilities, which grow exponentially until they come into conflict with the assumptions of the hard-loop approximation (namely that the fields have only small effects on the trajectories of the hard particles), whereupon isotropization is supposed to set in.

Apart from a brief transitory slowdown, the 1+1-dimensional simulations thus evolve similarly to Abelian instabilities both in the linear and the strongly nonlinear domain (at least as far as the dominant transverse components are concerned). A measure of local “non-Abelianness” can be defined by ⁷

$$\bar{C}[j] = \int_0^L \frac{dz}{L} \frac{\{\text{tr}((i[j_x, j_y])^2)\}^{1/2}}{\text{tr}(j_x^2 + j_y^2)}. \quad (45)$$

Indeed, when the nonlinear regime is entered, this quantity is found to decay roughly exponentially (with some hiccup brought out only with sufficiently large \mathcal{N}), but not as fast as it was found in the toy model of Ref. [24].

Ref. [24] also observed a concurrent global Abelianization, by comparing the correlation among parallel transported spatially separated commutators to the correlation of parallel transported fields. Generalizing the quantity used in Ref. [24],⁸ we define

$$\chi_A(\xi) = \frac{N_c^2 - 1}{2N_c} \int_0^L \frac{dz}{L} \frac{\text{tr} \{ (i[j_i(z + \xi), \mathcal{U}(z + \xi, z)j_j(z)])^2 \}}{\text{tr} \{ j_k^2(z + \xi) \} \text{tr} \{ j_l^2(z) \}} \quad (46)$$

⁷ This definition coincides with the definition in Ref. [24] in the simplifying case (43), but is gauge invariant in the full theory also when the restriction to 1+1 dimensional configurations is removed.

⁸ We use currents instead of transverse gauge field components, because they transform like adjoint matter when the restriction to 1+1-dimensional situations is removed.

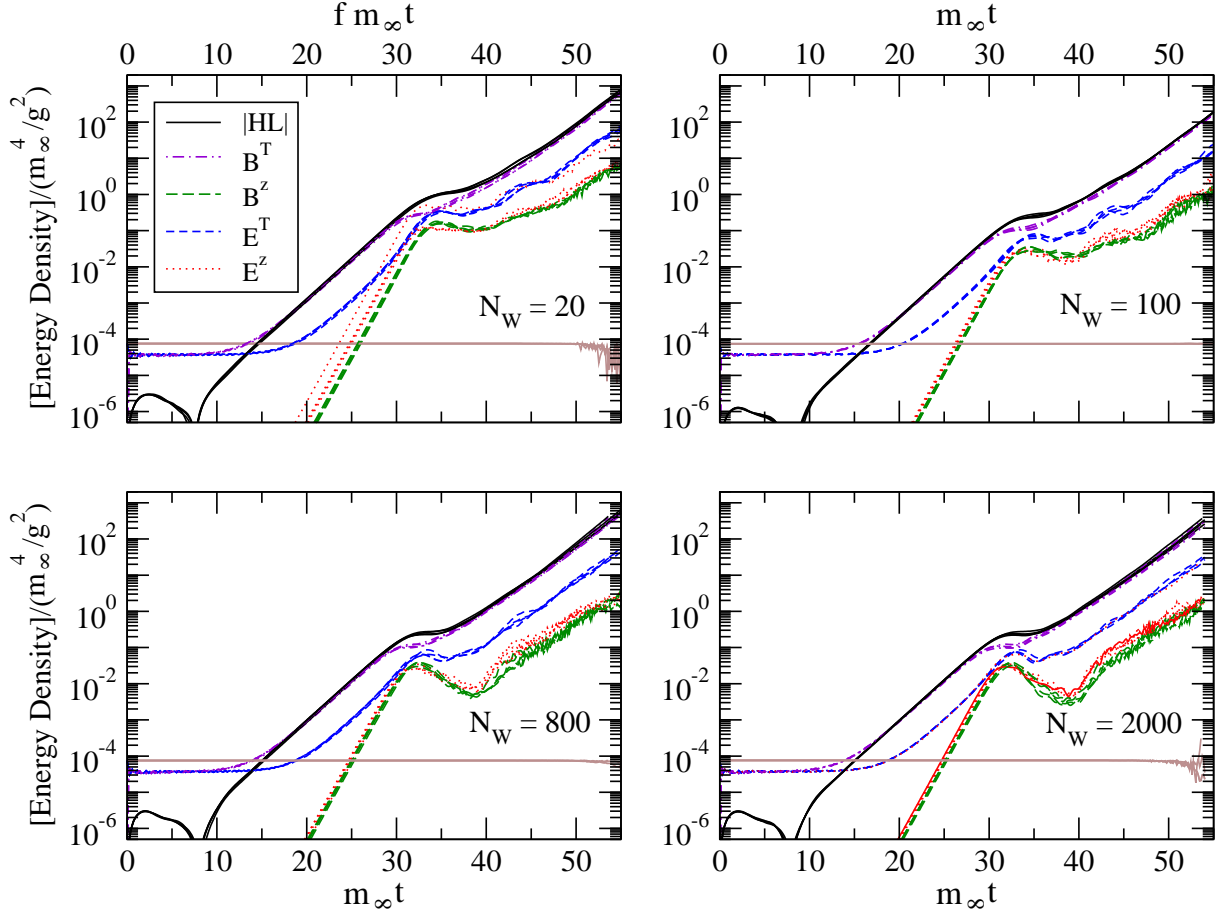


FIG. 6: Average energy densities \mathcal{E} in transverse/longitudinal chromomagnetic/electric fields and the total energy density contributed by hard particles, $\mathcal{E}(\text{HL})$, for various values of \mathcal{N} . In the case $\mathcal{N} = 20$, where there is a noticeable difference between γ_* at the discretized level from the continuum value (see middle plot in Fig. 2), we have rescaled the factor m_∞ in front of t by $f = \gamma_*(\mathcal{N} = 20)/\gamma_* = 1.29336$. The horizontal line terminating in fluctuations is the total conserved energy (7).

where $\mathcal{U}(z', z)$ is the adjoint-representation parallel transport from z to z' . When colors are completely uncorrelated over a distance ξ , this quantity equals unity; if they point in the same direction, this quantity vanishes. Following Ref. [24] we define the “Abelianization correlation length” ξ_A as the smallest distance where χ_A is larger than $1/2$,

$$\xi_A[j] = \min_{\chi_A(\xi) \geq 1/2} (\xi). \quad (47)$$

This we compare with a general correlation length, not focussing on color, defined through the gauge invariant function

$$\chi(\xi) = \frac{\int_0^L \frac{dz}{L} \text{tr} \{j_i(z + \xi) \mathcal{U}(z + \xi, z) j_i(z)\}}{\int_0^L \frac{dz}{L} \text{tr} \{j_i(z) j_i(z)\}}. \quad (48)$$

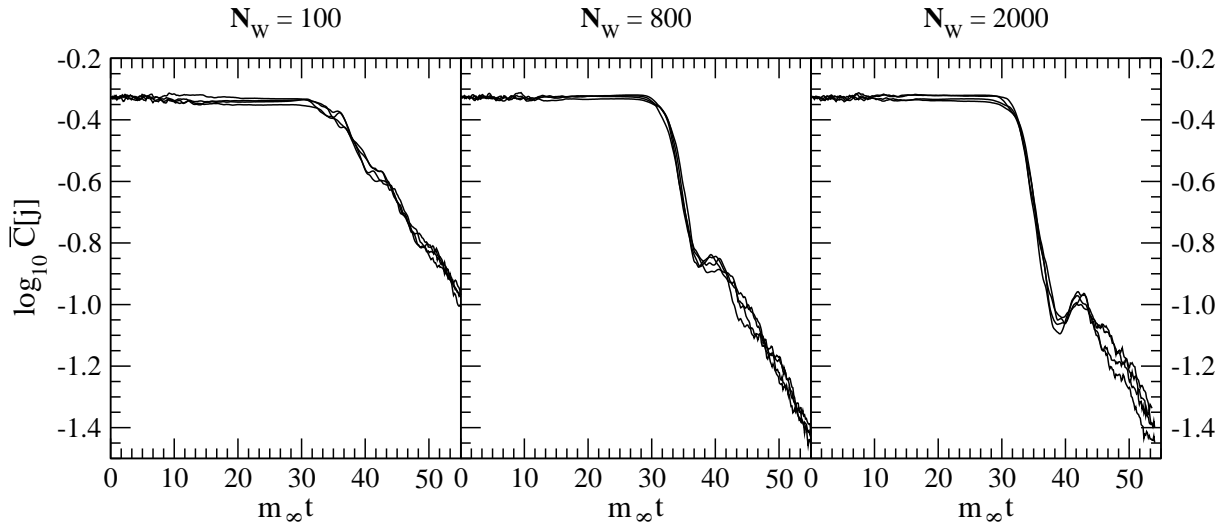


FIG. 7: The relative rms size \bar{C} of commutators $[j_x, j_y]$ as a function of time for $\mathcal{N} = 100, 800, 2000$.

This function now vanishes when fields are uncorrelated over a distance ξ , and it is normalized such that $\chi(0) = 1$. We thus define the general correlation length through

$$\xi[j] = \min_{\chi(\xi) \leq 1/2}(\xi). \quad (49)$$

The evolution of the general and the Abelianization correlation length is shown in Fig. 8. In contrast to the toy model of Ref. [24], where ξ_A was found to rapidly grow to full lattice size when \bar{C} begins its decay (while no such behavior was seen in general correlation lengths), we find that Abelianization takes place only over domains of limited sizes, see Fig. 8. Deeper in the nonlinear regime, ξ_A is seen to have magnitudes comparable to the wavelength of the modes of maximal growth,⁹ $\lambda_* = 2\pi/k_* \approx 7.06 m_\infty^{-1}$.

In this regime, the different simulations with different \mathcal{N} agree fairly well, only in the transition region between linear and nonlinear regime it is essential to have higher values of \mathcal{N} to bring out an initial peak in the evolution of ξ_A .

C. Extension to gauge group SU(3)

The above numerical simulations have been performed with gauge group SU(2), which is the most economical in computer time. There is no particular reason why non-Abelian plasma instabilities should strongly depend on the gauge group (in particular when local Abelianization occurs). Nevertheless, this needs to be checked. In this section we discuss the changes which occur when the gauge group is taken to be SU(3) instead of SU(2). Functionally, the algorithm is exactly the same with the only difference being the underlying

⁹ Note again that in the model of Ref. [24] k_* vanishes, which is presumably responsible for the different global behavior.

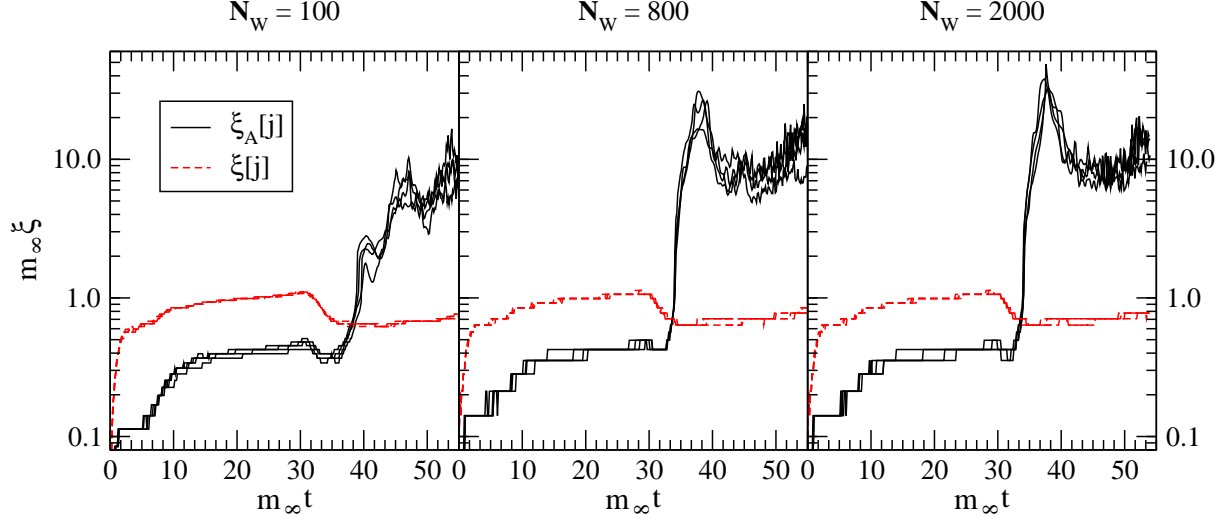


FIG. 8: The Abelianization correlation length $\xi_A[j]$ compared to the ordinary correlation length $\xi[j]$ for $\mathcal{N} = 100, 800, 2000$.

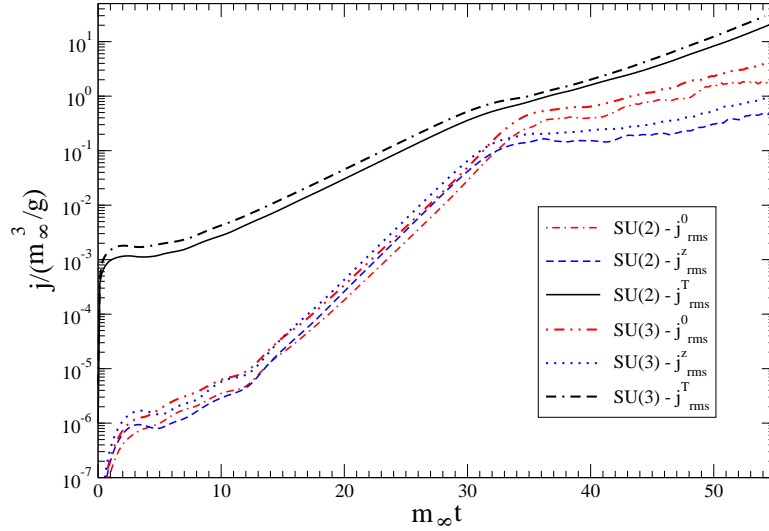


FIG. 9: The average current j_{rms}^\perp , j_{rms}^z and rms charge density j_{rms}^0 with gauge group SU(3) and SU(2), for one $\mathcal{N} = 100$ run each.

matrix representation for the fields. Figures 9 – 12 show the effect of upgrading the gauge group SU(2) to SU(3) for $\mathcal{N} = 100$.

In Figs. 9 and 10 we compare the results for the various current and energy components in the case of gauge group SU(3) with those for SU(2), both with $\mathcal{N} = 100$. Only minor differences are seen, with a little higher energies being reached in the nonlinear regime in SU(3), but that would need more extensive tests to be taken as a conclusion.

The amount of local and global Abelianization is shown in Figs. 11 and 12, respectively. Again, only small differences can be observed.

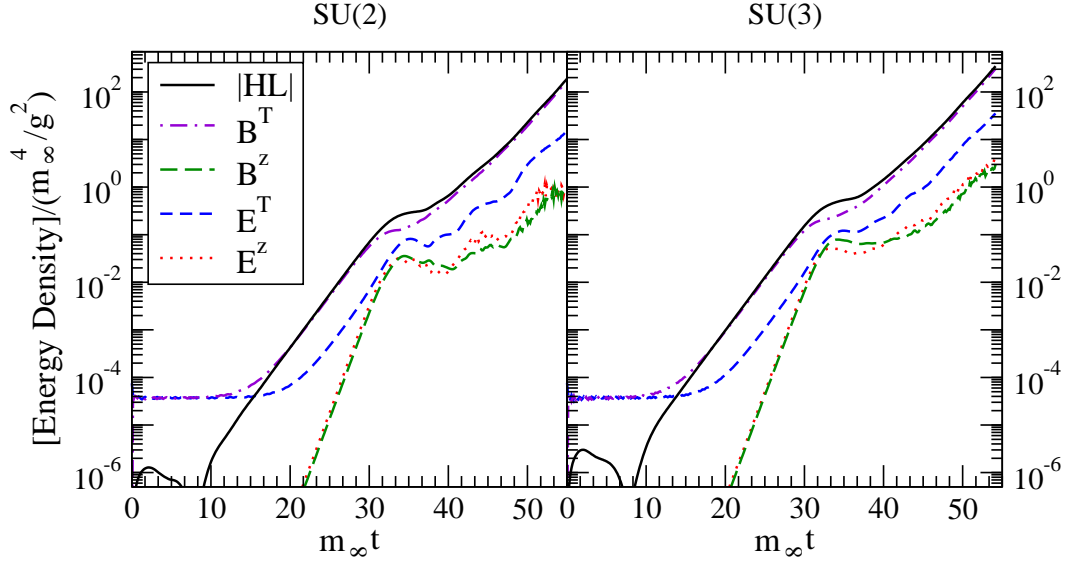


FIG. 10: SU(3) vs. SU(2) comparison of the average energy densities \mathcal{E} in transverse/longitudinal chromomagnetic/electric fields and the total energy density contributed by hard particles, $\mathcal{E}(\text{HL})$.

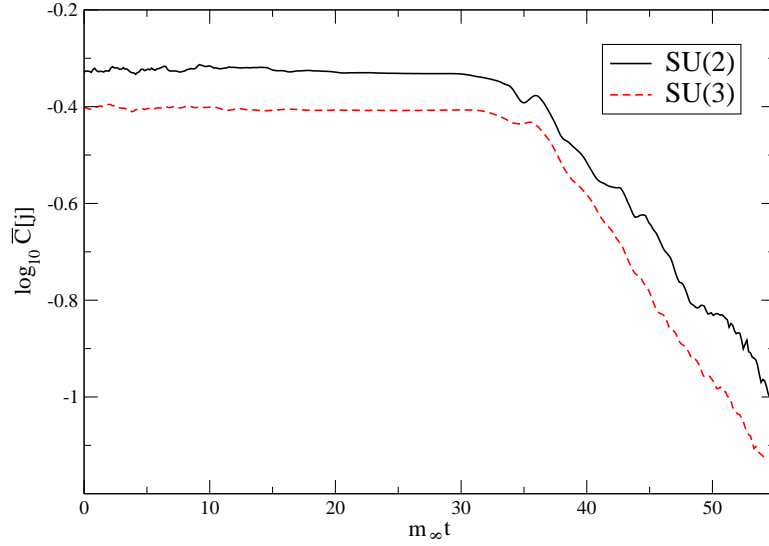


FIG. 11: SU(3) vs. SU(2) comparison of the local Abelianization measure \bar{C} of commutators $[j_x, j_y]$.

VI. 3+1-DIMENSIONAL LATTICE SIMULATIONS

We finally turn to the question to what extent relaxing strict translation invariance in transverse directions, which led to the great simplification of effectively 1+1-dimensional dynamics, does modify the evolution of plasma instabilities. In the linear regime, the time

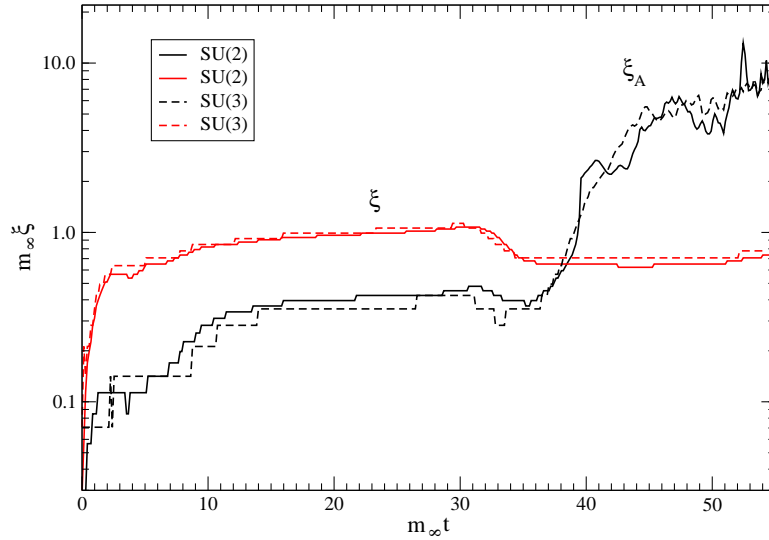


FIG. 12: SU(3) vs. SU(2) comparison of the Abelianization correlation length $\xi_A[j]$ together with the ordinary correlation length $\xi[j]$.

evolution favors the modes which are constant with respect to transverse directions, because these are the ones of largest growth. Thus, if one starts out with arbitrarily small seed fields, transverse translational symmetry will be arbitrarily well prepared for the subsequent nonlinear evolution (after correspondingly arbitrarily long Abelian evolution of course). This is the case that was covered by the previous section. However, generic initial conditions that take a finite time to evolve into the nonlinear regime (or start out there) will always have some breaking of transverse translational symmetry, and then one has to simulate full 3+1 dimensional dynamics to take this into account.

Figures 13–16 show our first results of such 3+1-dimensional lattice simulations. In these simulations we have no longer set up initial conditions corresponding only to transverse electric fields, but formulated these initial conditions in terms of the \mathcal{W} fields, see Eq. (B20).

We have investigated both asymmetrical and symmetrical lattices, but here we only present results from symmetric ones. In Fig. 13 we plot the resulting energy densities for a 96^3 lattice and the icosahedral approximation, $\mathcal{N} = 20$, compared to a one-dimensional simulation using the same parameters. As can be seen from this figure, differences from the one-dimensional simulations begin to appear at $m_\infty t \sim 35$ which is when the field amplitudes have reached order m_∞/g . The chosen lattice spacing corresponds to $a = 0.28m_\infty^{-1}$ so that the physical volume of the lattice is roughly $(28/m_\infty)^3$. In Fig. 14 we compare the energy densities obtained using $\mathcal{N} = 20, 100, 200$, namely the icosahedron and disco-balls with $\mathcal{N}_z \times \mathcal{N}_\varphi = 20 \times 5$ and 25×8 , with lattice sizes 96^3 , 88^3 , and 69^3 , respectively. The thick lines are the energy extracted from the hard particles (HL energy) and the other various components of the total energy are shown for comparison but not labelled explicitly. As can be seen from this figure there is general agreement between all three discretizations, the chief difference being that for late times the then approximately linear growth rate seems to decrease with increasing \mathcal{N} . The fluctuations in the overall amplitude are due to the different random initial conditions used for each run.

In the linear regime, i.e. field amplitudes $\ll m_\infty/g$, the differences are only due to the

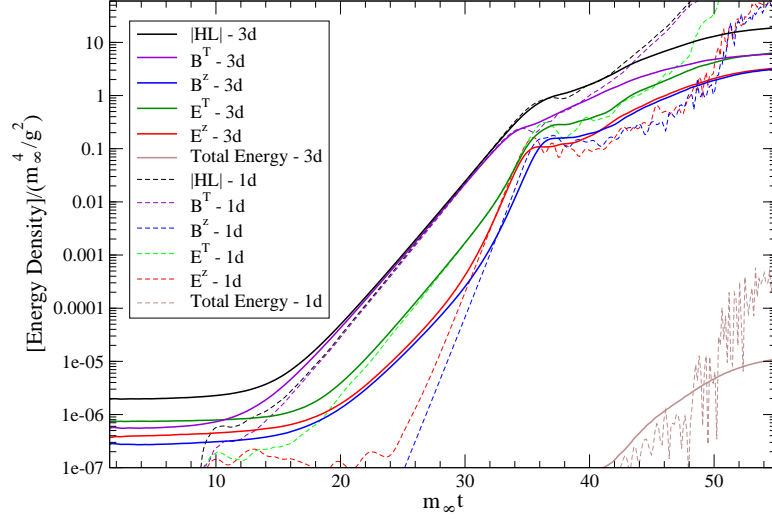


FIG. 13: Average energy densities \mathcal{E} in transverse/longitudinal chromomagnetic/electric fields and the total energy density contributed by hard particles, $\mathcal{E}(\text{HL})$ for 3+1-dimensional $\mathcal{N} = 20$.

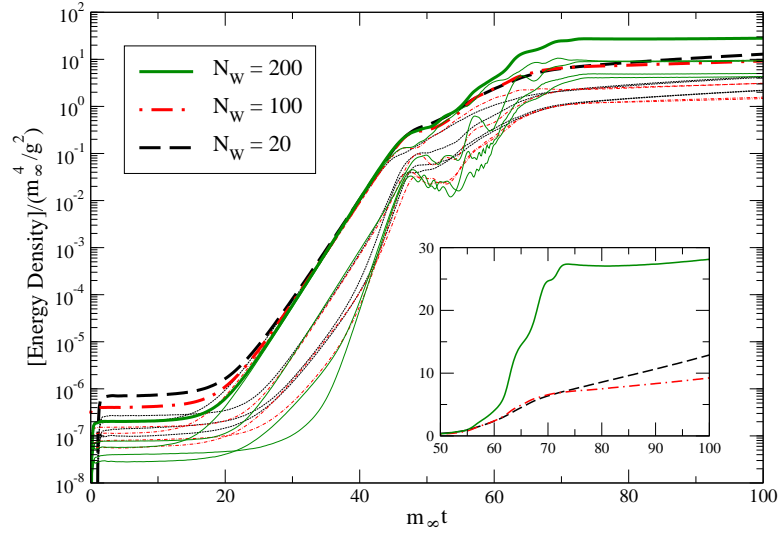


FIG. 14: Comparison of average energy densities \mathcal{E} for 3+1-dimensional simulations with $\mathcal{N} = 20, 100, 200$ on $96^3, 88^3, 69^3$ lattices. Thick lines correspond to $\mathcal{E}(\text{HL})$ and thin lines are the components which can be inferred from Fig. 15. In the case $\mathcal{N} = 20$ we have rescaled $m_\infty \rightarrow f m_\infty$ with $f = \gamma_*(\mathcal{N} = 20)/\gamma_* = 1.29336$ in order to properly normalize the results for comparison. In addition, we shifted the $\mathcal{N} = 20$ data 0.9 units in $m_\infty t$ to the right and the $\mathcal{N} = 100$ by 0.1 units in $m_\infty t$ to the left in order to roughly align the exponential-growth phase in the Abelian regime. Inset shows late-time behavior of the hard-loop energy density with a linear scale.

different amount of initial energy densities in longitudinal and transverse components. In both the 3+1-dimensional and the 1+1-dimensional case, the dominant component is from transverse magnetic fields, followed by transverse electric fields (suppressed by a factor of

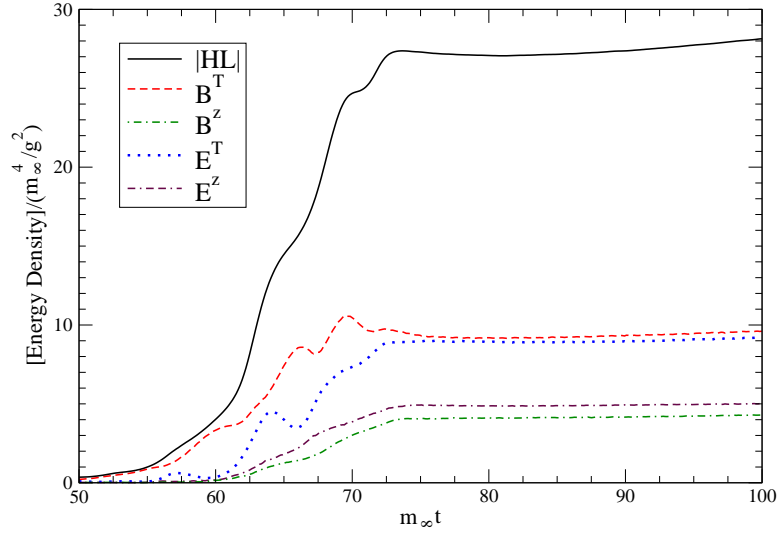


FIG. 15: Average energy densities \mathcal{E} in transverse/longitudinal chromomagnetic/electric fields and the total energy density contributed by hard particles, $\mathcal{E}(\text{HL})$ for 3+1-dimensional $\mathcal{N} = 200$, in linear scale.

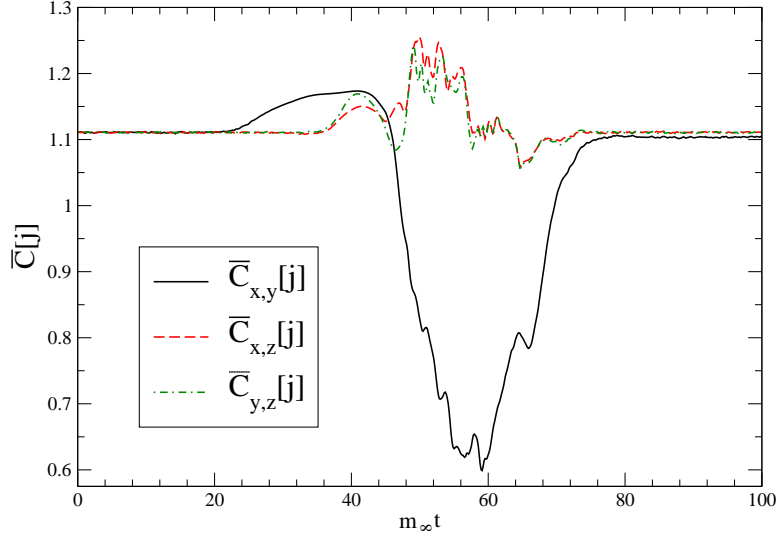


FIG. 16: The relative rms size of commutators $\bar{C}_{i,j}^2 = \text{tr}([j_i, j_j])^2 / (\text{tr} j_i^2 \text{tr} j_j^2)$ as a function of time compared for 3+1-dimensional versus 1+1-dimensional evolution with $\mathcal{N} = 200$.

$(\gamma_*/k_*)^2 < 1$. Longitudinal components are initially absent in the 1+1-dimensional preparation of the system, but not in the full 3+1-dimensional case because of the different initial conditions (B20). Nevertheless, at the later stages of the linear evolution, they behave rather similarly. The regime where specifically non-Abelian effects come into the play first is also very similar in the two cases, and remain so for a while. However, whereas the 1+1-dimensional modes eventually recover their initial growth rates of the linear regime, the

transversely nonconstant modes seem to be the determining factor deeper into the nonlinear regime, and these behave rather differently from the former. In Figs. 13 and 14 one sees subexponential behavior at late times, which in fact seems to tend to a linear growth at large times. This can be seen most clearly in Fig. 15 where we plot the components of the energy density at late times on a linear scale for a 69^3 lattice and $\mathcal{N} = 200$. The chosen lattice spacing corresponds to $a = 0.28m_\infty^{-1}$ so that the physical volume of the lattice is roughly $(19/m_\infty)^3$.

This finding is in agreement with the most recent results by Arnold, Moore, and Yaffe [26], using a different discretization method for the hard-loop effective theory (namely truncation of expansions in spherical harmonics). While Ref. [26] presented a very extensive analysis of possible systematic uncertainties, our results, obtained with cruder discretizations, are still somewhat preliminary and require further systematic studies. Nevertheless, we already find agreement also in some of the finer details, such as the relative importance of longitudinal field components in the late time evolution.

In Fig. 16 we moreover display results for the normalized size of the commutators $\bar{C}_{i,j}^2 = \text{tr}([j_i, j_j])^2 / (\text{tr} j_i^2 \text{tr} j_j^2)$ which give a measure of local Abelianization with respect to the three possible spatial directions. As can be seen from this figure there is initially Abelianization in the xy commutator starting at $m_\infty t \sim 40$, while the other two commutators show no evidence for Abelianization. At later times ($m_\infty t > \sim 60$), the xy commutator becomes less and less abelian and at late times, in the linear-growth phase, the soft-current commutators are nearly isotropic.

VII. CONCLUSION AND OUTLOOK

In this paper we have presented detailed results from our numerical studies of discretized hard loops applied to the time-evolution of quark-gluon plasma instabilities due to momentum space anisotropy. We extended our previous effective 1+1 dimensional analysis to include the SU(3) gauge group finding that the results obtained for SU(3) were qualitatively similar to those of our SU(2) simulations. In addition, we have presented first results for the full 3+1 dimensional evolution of the system using our method to discretize the hard-loop effective theory. We tentatively confirm the results of Arnold, Moore, and Yaffe [26] who find linear instead of exponential growth of the hard-loop energy at late times.

The fact that 3+1 dimensional nonabelian plasma instabilities seem to nearly saturate in the nonlinear regime where field amplitudes are of order m_∞/g makes it even more interesting and also self-consistent to study their dynamics and their role in isotropization and thermalization of quark-gluon plasma within discretized hard-loop approximations. A more extensive and thorough study of 3+1 dimensional quark-gluon-plasma instabilities will be the subject of a forthcoming publication.

Acknowledgments

We thank P. Arnold, D. Bödeker, M. Laine, G. Moore, and L. Yaffe for valuable discussions. M.S. was supported by the Academy of Finland, contract no. 77744. P.R. was supported by the DFG-Forschergruppe EN 164/4-4.

APPENDIX A: SMALL ξ EXPANSION OF DISPERSION LAWS

1. Continuum results

The small- ξ expansion of the continuum transverse plasma frequency (25) reads

$$\omega_{pl,t}^2/m^2 = \underbrace{\frac{1}{3}}_{p_1} - \underbrace{\frac{2}{15}}_{p_2} \xi + \underbrace{\frac{3}{35}}_{p_3} \xi^2 + O(\xi^3). \quad (\text{A1})$$

(The coefficients p_k are compared with the \mathbf{v} -discretized results in Table II).

Propagating modes with small k are characterized by

$$\omega_t^2(k) = \omega_{pl,t}^2 + \left[\underbrace{\frac{5}{6}}_{q_1} + \underbrace{\frac{19}{175}}_{q_2} \xi + O(\xi^2) \right] k^2 + O(k^4). \quad (\text{A2})$$

The small- ξ expansion of the asymptotic mass (26) of the transverse excitations reads

$$m_\infty^2/m^2 = \underbrace{\frac{1}{2}}_{r_1} - \underbrace{\frac{1}{6}}_{r_2} \xi + \underbrace{\frac{1}{10}}_{r_3} \xi^2 + O(\xi^3). \quad (\text{A3})$$

The plasma frequency in the longitudinal sector, Eq. (29), has the expansion

$$\omega_{pl,\ell}^2/m^2 = \underbrace{\frac{1}{3}}_{s_1} - \underbrace{\frac{1}{15}}_{s_2} \xi + \underbrace{\frac{1}{35}}_{s_3} \xi^2 + O(\xi^3). \quad (\text{A4})$$

2. Discretized hard loops

Table II shows how well the coefficients p_k, q_k, r_k of the small- ξ expansion of the above parameters in the dispersion laws are reproduced with \mathbf{v} -discretized hard loops. In the case of regular polyhedra, more and more coefficients p_k, q_k, r_k become exact or come closer to the continuum result as \mathcal{N} increases. For the two pairs of polyhedra where the dispersion laws coincide, there is particular good agreement with the continuum results for the asymptotic transverse masses, however at the expense of having one coefficient with a wrong sign in the longitudinal sector.

The lower part of Table II performs the same¹⁰ comparison for a few cases of the “disco-ball” discretization (16) with regular spacing in z and φ . For $\mathcal{N} \leq 20$, the regular polyhedra turn out to be superior in the small- ξ expansion. However, the disco-ball discretization allows us to increase \mathcal{N} without limit, and while (with the exception of r_1) no coefficient becomes exact, all of them can be systematically improved. For example, choosing $N_z = 16$ or 32 improves the coefficient p_1 to become accurate to 0.2% or 0.05%, respectively.

The relation (27) between the transverse plasma frequency and the static mass parameter μ^2 which determines the range of plasma instabilities is in fact exact in all cases we have considered, so the coefficients p_k in Table II cover both the transverse plasma frequency and the magnetic instability (resp. screening) mass scale for $\xi > 0$ ($\xi < 0$).

¹⁰ The coefficients $q_{1,2}$ have been omitted out of laziness.

TABLE II: A comparison of parameters characterizing the dispersion laws in anisotropic plasmas at small anisotropy parameter ξ between continuum and \mathbf{v} -discretized hard loops. The upper part of the table refers to discretization by regular polyhedra $\mathcal{N} = 6, 8, 12, 20$ with different orientations and hence different discrete (Z_φ) rotational symmetry around the z -axis and different numbers N_z of distinct values v_z . The numbers on the right-hand side give the factors by which the coefficients defined in (A1), (A2), (A3), (A4) differ from the exact ones. These factors are given only up to the first term where there is a deviation from the exact result. The lower entries correspond to the “disco-ball” discretization (16) with regular spacing in z and φ (there the results actually only depend on N_z if $N_\varphi \geq 2$).

\mathcal{N}	Z_φ	N_z	p_1	p_2	p_3	q_1	q_2	r_1	r_2	r_3	s_1	s_2	s_3
6	4	3	1	0		0		1.50	0		1	5.00	
6	3	2	1	1.67		1.11		1	1	0.56	1	-1.67	
8	4	2	1	1.67		1.11		1	1	0.56	1	-1.67	
8	3	4	1	0.56		0.93		0.75			1	2.78	
12	5	4	1	1	0.47	1	1.84	0.83			1	1	4.20
12	3	4	1	1	1.30	1	0.53	1	1	1	1	1	-0.78
20	5	4	1	1	1.30	1	0.53	1	1	1	1	1	-0.78
20	3	6	1	1	0.84	1	1.26	0.90			1	1	1.99
8	4	2	1.13	1.41				1	0.75	0.31	0.75	-1.88	
20	5	4	1.03	1.14	1.24			1	0.94	0.80	0.94	0.12	-1.85
32	4	8	1.008	1.04	1.08			1	0.98	0.95	0.98	0.77	

APPENDIX B: LATTICE EQUATIONS OF MOTION

1. 1+1-dimensional case

In the dimensionally reduced situation arising for initial conditions depending only on z and t , we have adjoint scalar fields $\phi_x = A_x$ and $\phi_y = A_y$ as well as auxiliary fields $\mathcal{W}_\mathbf{v}$ in the adjoint representation, which live on the sites of the spatial lattice with lattice spacing a . These are represented as $N_c \times N_c$ traceless Hermitian matrices belonging to the Lie algebra of $\text{SU}(N_c)$. Furthermore there are the conjugate momenta π_x and π_y (corresponding to $\partial_t A_x$ and $\partial_t A_y$) and $E_z = -\partial_t A_z$ which are all represented as $N_c \times N_c$ traceless Hermitian matrices living on the temporal links. Finally, there are $\text{SU}(N_c)$ group elements U which live on the spatial links. The latter represent the discretized version of the parallel transporter which in fundamental representation is given by

$$U(z', z) = \mathcal{P} \exp \left(-ig \int_z^{z'} dz'' A_z(z'') \right) \quad (\text{B1})$$

and where \mathcal{P} represents path ordering (with z' to the left and z on the right). The discretized version then transports from the site z to the site $z' = z + a \rightarrow s + 1$, so that

$$U_{s+\frac{1}{2}} = \exp(-igaA_{z,s}). \quad (\text{B2})$$

The covariant derivative D_z may then be discretized into a right-transporting and a left-transporting version,

$$D_z^R \phi_s \rightarrow \frac{\phi_s - U_{s-\frac{1}{2}} \phi_{s-1} U_{s-\frac{1}{2}}^\dagger}{a}, \quad D_z^L \phi_s \rightarrow \frac{U_{s+\frac{1}{2}}^\dagger \phi_{s+1} U_{s+\frac{1}{2}} - \phi_s}{a}, \quad (\text{B3})$$

whereas the second order derivative is then symmetric since

$$D_z^2 \rightarrow \frac{D_z^L - D_z^R}{a}. \quad (\text{B4})$$

Since the $E_{z,s}$ are living on the spatial links from s to $s+1$, the first order covariant derivative has to be taken as D_L , while the current is replaced by an average between the beginning and the end of the link. Specifically,

$$\begin{aligned} \pi_{\alpha,s}(t + \frac{\epsilon}{2}) &= \pi_{\alpha,s}(t - \frac{\epsilon}{2}) + \epsilon \left[a^{-1} (D_z^L - D_z^R) \phi_s - g^2 [\phi_{\bar{\alpha},s}, [\phi_{\bar{\alpha},s}, \phi_{\alpha,s}]] + j_{\alpha,s} \right]_t \\ E_{z,s}(t + \frac{\epsilon}{2}) &= E_{z,s}(t - \frac{\epsilon}{2}) + \epsilon \left[ig \sum_{\alpha} [\phi_{\alpha,s}, D_z^L \phi_{\alpha,s}] - \frac{1}{2} \left(j_{z,s} + U_{s+\frac{1}{2}}^\dagger j_{z,s+1} U_{s+\frac{1}{2}} \right) \right]_t, \end{aligned} \quad (\text{B5})$$

where α runs over x, y and $\bar{\alpha}$ denotes y and x . The fields are then updated using symmetric first order spatial derivatives ($D_z \rightarrow D_z^S = (D_z^L + D_z^R)/2$),

$$\begin{aligned} \phi_{\alpha,s}(t + \epsilon) &= \phi_{\alpha,s}(t) + \epsilon \pi_{\alpha,s}(t + \frac{1}{2}\epsilon) \\ \mathcal{W}_{\mathbf{v},s}(t + \epsilon) &= \mathcal{W}_{\mathbf{v},s}(t) + \epsilon \left[-ig[\mathcal{A}(t), \mathcal{W}_{\mathbf{v}}(t)] + b_{\mathbf{v}} D_z^S \mathcal{A}(t) - v_z D_z^S \mathcal{W}_{\mathbf{v},s}(t) - a_{\mathbf{v}} v_x \pi_x(t + \frac{\epsilon}{2}) \right. \\ &\quad \left. - a_{\mathbf{v}} v_y \pi_y(t + \frac{\epsilon}{2}) \right]_s + \epsilon \left[\frac{E_{z,s}(t + \frac{\epsilon}{2}) + U_{s-\frac{1}{2}}(t) E_{z,s-1}(t + \frac{\epsilon}{2}) U_{s-\frac{1}{2}}^\dagger(t)}{2} (v_z a_{\mathbf{v}} + b_{\mathbf{v}}) \right] \\ \mathcal{A}(t) &= v_x \phi_x(t) + v_y \phi_y(t). \end{aligned} \quad (\text{B6})$$

Finally, choosing $E_{z,s}$ to transform at the spatial lattice site s rather than $s+1$ we find for the following update law for the links U :

$$U_{s+\frac{1}{2}}(t + \epsilon) = U_{s+\frac{1}{2}}(t) \exp \left(ig \epsilon a E_{z,s}(t + \frac{\epsilon}{2}) \right). \quad (\text{B7})$$

Gauss's law becomes

$$ig \sum_{\alpha} [\phi_{\alpha,s}(t), \pi_{\alpha,s}(t - \frac{\epsilon}{2})] - D_z^R E_{z,s}(t - \frac{\epsilon}{2}) + \frac{1}{N} \sum_{\mathbf{v}} \mathcal{W}_{\mathbf{v},s}(t) = 0 \quad (\text{B8})$$

while the approximately conserved energy (7) is discretized by

$$\begin{aligned} \mathcal{E} &= a \sum_s \left\{ \frac{1}{4} \text{tr} \left[\left(E_{z,s}(t - \frac{\epsilon}{2}) + E_{z,s}(t + \frac{\epsilon}{2}) \right)^2 \right] + \sum_{\alpha} \left[\frac{1}{4} \text{tr} \left[\left(\pi_{\alpha,s}(t - \frac{\epsilon}{2}) + \pi_{\alpha,s}(t + \frac{\epsilon}{2}) \right)^2 \right] \right. \right. \\ &\quad \left. \left. + \text{tr} \left((D_z^R \phi_{\alpha,s}(t))^2 \right) \right] + \text{tr} \left((i[\phi_{x,s}, \phi_{y,s}])^2 \right)_t + \epsilon \sum_{t'=0}^t \text{tr} \left[-\pi_{x,s}(t' - \frac{\epsilon}{2}) (j_{x,s}(t' - \epsilon) + j_{x,s}(t')) \right. \right. \\ &\quad \left. \left. - \pi_{y,s}(t' - \frac{\epsilon}{2}) (j_{y,s}(t' - \epsilon) + j_{y,s}(t')) + \frac{1}{2} \left(E_{z,s}(t' - \frac{\epsilon}{2}) + U_{s-\frac{1}{2}}(t') E_{z,s-1}(t' - \frac{\epsilon}{2}) U_{s-\frac{1}{2}}^\dagger(t') \right) \right. \right. \\ &\quad \left. \left. (j_{z,s}(t' - \epsilon) + j_{z,s}(t')) \right] \right\}, \end{aligned} \quad (\text{B9})$$

As initial conditions we choose

$$U_{s+\frac{1}{2}}(0) = \mathbf{1}_{N_c}, \quad \phi_{\alpha,s}(0) = 0, \quad E_{z,s}(-\frac{\epsilon}{2}) = 0, \quad \mathcal{W}_{\mathbf{v},s}(0) = 0, \\ \langle \pi_{\alpha,s}^a(-\frac{\epsilon}{2}) \pi_{\beta,s'}^b(-\frac{\epsilon}{2}) \rangle = \sigma^2 \delta^{ab} \delta_{\alpha\beta} \delta_{ss'} / a \quad . \quad (\text{B10})$$

Under local gauge transformations $\Lambda(z)$ one has

$$\begin{aligned} \phi_{\alpha,s} &\rightarrow \phi'_{\alpha,s} = \Lambda_s \phi_{\alpha,s} \Lambda_s^{-1} \\ \pi_{\alpha,s} &\rightarrow \pi'_{\alpha,s} = \Lambda_s \pi_{\alpha,s} \Lambda_s^{-1} \\ E_{z,s} &\rightarrow E'_{z,s} = \Lambda_s E_{z,s} \Lambda_s^{-1} \\ \mathcal{W}_{\mathbf{v},s} &\rightarrow \mathcal{W}'_{\mathbf{v},s} = \Lambda_s \mathcal{W}_{\mathbf{v},s} \Lambda_s^{-1} \\ U_{s+\frac{1}{2}} &\rightarrow U'_{s+\frac{1}{2}} = \Lambda_{s+1} U_{s+\frac{1}{2}} \Lambda_s^{-1} \end{aligned} \quad (\text{B11})$$

which can be used to check explicit gauge invariance of the results.

2. 3+1-dimensional case

For the 3+1 dimensional simulation, we found it convenient to follow very closely the lattice equations of motion used in Ref. [31]. The dynamical variables are taken to be the three electric fields $E_i(x) = -\partial_t A_i(x)$, lattice links $U_i(x) = \exp(-igaA_i)$ and the auxiliary fields $\mathcal{W}_{\mathbf{v}}(x)$. Sticking to the convention of Ref. [31], this unfortunately creates a slight inconsistency with the definition of the links U_i in the last subsection: for the three dimensional simulation, these are now defined to transport from site \vec{x} to site $\vec{x} - a\hat{e}_i$. Furthermore, we make the field variables dimensionless by absorbing the lattice spacing as well as the strong coupling constant g by

$$gaA \rightarrow A, \quad ga^a E \rightarrow E, \quad ga^3 \mathcal{W} \rightarrow \mathcal{W}, \quad ga^3 j \rightarrow j. \quad (\text{B12})$$

Making use of the shorthand notation $\mathbf{x} + a\hat{e}_i \rightarrow x + i$, the lattice equations of motion then read for gauge group SU(2)

$$\begin{aligned} E_i^a(t + \frac{\epsilon}{2}, x) &= E_i(t - \frac{\epsilon}{2}, x) + 2i\epsilon \operatorname{tr} \left(\tau^a U_i(t, x) \sum_{|j| \neq i} S_{ij}^\dagger(t, x) \right) \\ &\quad - \frac{\epsilon}{2} \left(j_i(t, x) + U_i(t, x) j_i(t, x + i) U_i^\dagger(t, x) \right) \\ U_i(t + \epsilon, x) &= \exp \left(i \epsilon E_i(t + \frac{\epsilon}{2}, x) \right) U_i(t, x) \end{aligned} \quad (\text{B13})$$

$$\begin{aligned} \mathcal{W}_{\mathbf{v}}^a(t + \epsilon, x) &= \mathcal{W}_{\mathbf{v}}^a(t, x) - \epsilon \mathbf{v} \cdot \mathbf{D}_S \mathcal{W}_{\mathbf{v}}^a(t, x) + \epsilon (a_{\mathbf{v}} \mathbf{v} + b_{\mathbf{v}} \hat{\mathbf{e}}_z) \cdot \mathbf{E}^a(t + \frac{\epsilon}{2}) \\ &\quad - 2i\epsilon b_{\mathbf{v}} (v_x \operatorname{tr}(\tau^a U_{\square, xz}(t, x)) + v_y \operatorname{tr}(\tau^a U_{\square, yz}(t, x))), \end{aligned} \quad (\text{B14})$$

where

$$S_{ij}^\dagger(t, x) = U_j(t, x + i) U_i^\dagger(t, x + j) U_j^\dagger(t, x) \quad (\text{B15})$$

is the gauge link staple,

$$U_{\square, ij}(t, x) = U_i(t, x) U_j(t, x + i) U_i^\dagger(t, x + j) U_j^\dagger(t, x) \quad (\text{B16})$$

is the standard plaquette and the symmetric covariant derivative here is now

$$D_i^S \phi(t, x) = \frac{1}{2} \left(U_i(t, x) \phi(t, x + i) U_i^\dagger(t, x) - U_i^\dagger(t, x - i) \phi(t, x - i) U_i(t, x - i) \right). \quad (\text{B17})$$

Note that the sum $\sum_{|j| \neq i}$ runs over both positive and negative directions, with $U_{-j}(t, x) = U_j^\dagger(x - j)$.

Contrary to Ref. [31] we did not discretize the first order temporal derivatives in a symmetric way, thereby breaking explicit time reversal symmetry which might introduce additional lattice discretization artifacts in the simulation. However, by using different temporal step sizes and different lattice spacings we have convinced ourselves that our results are afflicted only very mildly by these artifacts if we choose ϵ/a sufficiently small.

The energy density (7) then reads

$$\begin{aligned} \mathcal{E} = & \frac{1}{g^2 a^4} \left[4 \sum_{\square} \left(1 - \frac{1}{2} \text{tr} U_{\square}(t, x) \right) + \frac{1}{4} \sum_i \text{tr} \left(E_i(t - \frac{\epsilon}{2}, x) + E_i(t + \frac{\epsilon}{2}, x) \right)^2 + \right. \\ & \epsilon \sum_i \sum_{t'=0}^t \text{tr} E_i(t' - \frac{\epsilon}{2}, x) \left(j(t' - \epsilon, x) + j(t', x) + U_i(t', x) j(t' - \epsilon, x + i) U_i^\dagger(t', x) \right. \\ & \left. \left. + U_i(t', x) j(t', x) U_i^\dagger(t', x) \right) \right], \end{aligned} \quad (\text{B18})$$

and Gauss's law becomes

$$\sum_i \left(U_i^\dagger(t, x - i) E_i(t - \frac{\epsilon}{2}, x - i) U_i(t, x - i) - E_i(t - \frac{\epsilon}{2}, x) \right) + \frac{1}{\mathcal{N}} \sum_{\mathbf{v}} \mathcal{W}_{\mathbf{v}}(t, x) = 0. \quad (\text{B19})$$

Finally, we initialize our three-dimensional simulations with $E_i(-\frac{\epsilon}{2}, x) = A_i(0, x) = 0$ and

$$\langle \mathcal{W}_{\mathbf{v}}^a(0, x) \mathcal{W}_{\mathbf{v}}^b(0, y) \rangle = \delta^{ab} \delta_{x,y}^3 \sigma^2 a^3, \quad (\text{B20})$$

where $\delta_{x,y}^3$ denotes 3 Kronecker deltas, and subtract $\sum_{\mathbf{v}} \mathcal{W}^a / \mathcal{N}^2$ from each \mathcal{W}^a in order to obey Gauss's law.

-
- [1] S. M. H. Wong, *Phys. Rev.* **C54**, 2588 (1996); *ibid.* **C56**, 1075 (1997). R. Baier, A. H. Mueller, D. Schiff and D. T. Son, *Phys. Lett. B* **502**, 51 (2001); A. H. Mueller, A. I. Shoshi and S. M. H. Wong, "A possible modified 'bottom-up' thermalization in heavy ion collisions," arXiv:hep-ph/0505164.
 - [2] D. Molnar and M. Gyulassy, *Nucl. Phys. A* **697**, 495 (2002) [Erratum-*ibid.* A **703**, 893 (2002)].
 - [3] U. W. Heinz, arXiv:nucl-th/0407067.
 - [4] A. Peshier and W. Cassing, arXiv:hep-ph/0502138.
 - [5] Y. V. Kovchegov, "Can thermalization in heavy ion collisions be described by QCD diagrams?," arXiv:hep-ph/0503038.
 - [6] E. Shuryak, *J. Phys. G* **30**, S1221 (2004); E. V. Shuryak and I. Zahed, *Phys. Rev. C* **70**, 021901 (2004) [arXiv:hep-ph/0307267].
 - [7] P. Kovtun, D. T. Son and A. O. Starinets, *Phys. Rev. Lett.* **94**, 111601 (2005) [arXiv:hep-th/0405231].

- [8] H. Nastase, “The RHIC fireball as a dual black hole,” arXiv:hep-th/0501068.
- [9] D. Kharzeev and K. Tuchin, “From color glass condensate to quark gluon plasma through the event horizon,” Nucl. Phys. A **753**, 316 (2005) [arXiv:hep-ph/0501234].
- [10] E.S. Weibel, Phys. Rev. Lett. **2**, 83 (1959).
- [11] P. Romatschke and M. Strickland, Phys. Rev. D **68**, 036004 (2003) [arXiv:hep-ph/0304092].
- [12] P. Romatschke and M. Strickland, Phys. Rev. D **70**, 116006 (2004) [arXiv:hep-ph/0406188].
- [13] F. Califano, N. Attico, F. Pegoraro, G. Bertin and S. V. Bulanov, Phys. Rev. Lett. **86**, 5293 (2001).
- [14] S. Mrówczyński, Phys. Lett. B **214**, 587 (1988); Phys. Lett. B **314**, 118 (1993); Phys. Rev. C **49**, 2191 (1994); Phys. Lett. B **393**, 26 (1997).
- [15] U. W. Heinz, Nucl. Phys. A **418**, 603C (1984).
- [16] Y. E. Pokrovsky and A. V. Selikhov, JETP Lett. **47**, 12 (1988) [Pisma Zh. Eksp. Teor. Fiz. **47**, 11 (1988)]; Sov. J. Nucl. Phys. **52**, 146, 385 (1990) [Yad. Fiz. **52**, 229, 605 (1990)].
- [17] O. P. Pavlenko, Sov. J. Nucl. Phys. **55**, 1243 (1992) [Yad. Fiz. **55**, 2239 (1992)].
- [18] St. Mrówczyński and M. H. Thoma, Phys. Rev. D **62**, 036011 (2000) [arXiv:hep-ph/0001164].
- [19] J. Randrup and St. Mrówczyński, Phys. Rev. C **68**, 034909 (2003) [arXiv:nucl-th/0303021].
- [20] P. Arnold, J. Lenaghan, G. D. Moore and L. G. Yaffe, Phys. Rev. Lett. **94**, 072302 (2005) [arXiv:nucl-th/0409068].
- [21] P. Arnold, J. Lenaghan and G. D. Moore, JHEP **0308**, 002 (2003) [arXiv:hep-ph/0307325].
- [22] J. C. Taylor and S. M. H. Wong, Nucl. Phys. B **346**, 115 (1990); J. Frenkel and J. C. Taylor, Nucl. Phys. B **374**, 156 (1992); E. Braaten and R. D. Pisarski, Phys. Rev. D **45**, 1827 (1992).
- [23] S. Mrówczyński, A. Rebhan and M. Strickland, Phys. Rev. D **70**, 025004 (2004) [arXiv:hep-ph/0403256].
- [24] P. Arnold and J. Lenaghan, Phys. Rev. D **70**, 114007 (2004) [arXiv:hep-ph/0408052].
- [25] A. Rebhan, P. Romatschke and M. Strickland, Phys. Rev. Lett. **94**, 102303 (2005) [arXiv:hep-ph/0412016].
- [26] P. Arnold, G. D. Moore and L. G. Yaffe, “The Fate of Non-Abelian Plasma Instabilities in 3+1 Dimensions,” arXiv:hep-ph/0505212.
- [27] J. P. Blaizot and E. Iancu, Phys. Rept. **359**, 355 (2002) [arXiv:hep-ph/0101103]; U. Kraemmer and A. Rebhan, Rept. Prog. Phys. **67**, 351 (2004) [arXiv:hep-ph/0310337]; J. O. Andersen and M. Strickland, Annals Phys. **317**, 281 (2005) [arXiv:hep-ph/0404164].
- [28] J. P. Blaizot and E. Iancu, Nucl. Phys. B **417**, 608 (1994) [arXiv:hep-ph/9306294].
- [29] J. P. Blaizot and E. Iancu, Nucl. Phys. B **421**, 565 (1994).
- [30] A. Rajantie and M. Hindmarsh, Phys. Rev. D **60**, 096001 (1999).
- [31] D. Bödeker, G. D. Moore and K. Rummukainen, Phys. Rev. D **61**, 056003 (2000) [arXiv:hep-ph/9907545].
- [32] A. Dumitru and Y. Nara, “QCD plasma instabilities and isotropization,” arXiv:hep-ph/0503121.